applied sciences

MDPI

Article

Performance Analysis of an Open-Cathode PEM Fuel Cell System Under Dynamic Power Profiles Using an Energy-Based Approach

Teresa Donateo *, Andrea Graziano Bonatesta, Antonio Masciullo and Antonio Ficarella

Department of Engineering for Innovation, University of Salento, 73100 Lecce, Italy
* Correspondence: teresa.donateo@unisalento.it; Tel.: +39-0832-297-754

Featured Application

Air-cooled fuel cells for small Unmanned Aerial Vehicles (UAVs), ground robots, e-bikes, and light EV.

Abstract

Open-cathode Proton Exchange Membrane Fuel Cells (PEMFCs) are a promising technology for increasing the endurance of small Unmanned Aerial Vehicles (UAVs), ground robots, e-bikes, and light electric vehicles. However, their performance under realistic operating conditions is strongly influenced by rapid variations in load, temperature, and ambient pressure, which are often neglected in design-oriented or quasi-steady-state analyses. This study experimentally investigates a 1 kW open-cathode PEMFC system, including its balance of plant and a passive supercapacitor buffer, under a representative UAV flight power profile. Steady-state and dynamic tests were conducted to assess polarization characteristics, thermal behavior, parasitic power consumption, and hydrogen utilization. Results revealed significant thermal inertia and hysteresis effects during load transients, causing voltage deviations from steady-state performance and stabilization times exceeding 90 s. The supercapacitor effectively reduced stack current ramp rates, although some high-frequency oscillations remained. Under flight-representative conditions, the system achieved stable operation with average voltaic efficiency ranging from 55.3% to 60.7% and net efficiency ranging from 50.2% to 54.2%. Auxiliary components had a measurable impact on overall performance: cooling fans accounted for 2–6% of stack power during steady operation and approximately 2.5% of total mission energy, while hydrogen purge losses can significantly reduce vehicle endurance. The findings demonstrate the importance of energy-based performance assessment, including auxiliary loads and purge losses, to obtain realistic estimates of efficiency and endurance in dynamic PEMFC-powered applications.

Keywords: Proton Exchange Membrane Fuel Cell (PEMFC); dynamic operation; balance of plant (BOP); endurance and efficiency

Academic Editors: José Joaquín Linares León and Flávio Colmati

Received: 20 May 2026
Revised: 5 June 2026
Accepted: 9 June 2026
Published: 12 June 2026

1. Introduction

The hydrogen economy is one of today's most promising paths to obtaining cleaner energy and propulsion systems. For low-power applications like Unmanned Aerial Vehicles (UAVs) [1], ultralight vehicles [2,3], and ground robots [4,5]. Compared with other fuel-cell technologies like Direct-Methanol fuel cells [6], Proton Exchange Membrane Fuel Cells (PEMFCs) offer an advantageous combination of high power density, low operating

temperature, rapid start-up, and good dynamic response, making them particularly suitable for applications characterized by frequent load variations.

Open-cathode air-cooled fuel cells (often PEMFCs) are preferred for their simplicity, low weight, and passive air cooling/humidification when required power is below 6 kW [7]. By combining the superior energy density of hydrogen with the high specific power of lithium batteries and/or supercapacitors, propulsion systems with fuel cells can guarantee lower weights and longer ranges than batteries alone [8]. Compared with internal combustion engines fueled with hydrogen, fuel cells guarantee higher conversion efficiency and no direct emissions [9,10].

Figure 1 shows a generic schematic structure of a PEM fuel cell. At the core of a PEMFC lies the Membrane Electrode Assembly (MEA), interposed between the gas diffusion layers, which in turn separate the MEA from the reactant flow channels on both the anode and cathode sides [11]. Bipolar plates, sealing gaskets, and current collectors complete the cell. The cell converts the chemical energy of hydrogen into electricity with the following overall reaction:

$$H_2 + \frac{1}{2}O_2 \rightarrow H_2O + 286\ \text{kJ/mol} \quad (1)$$

During normal operation, the average voltage of a single cell ranges between 0.6 and 0.7 V. To achieve the required voltage, a certain number of cells are connected in series, forming a stack [12]. The nominal electric power of the stack depends on the active area of the MEA and the number of cells connected in series.

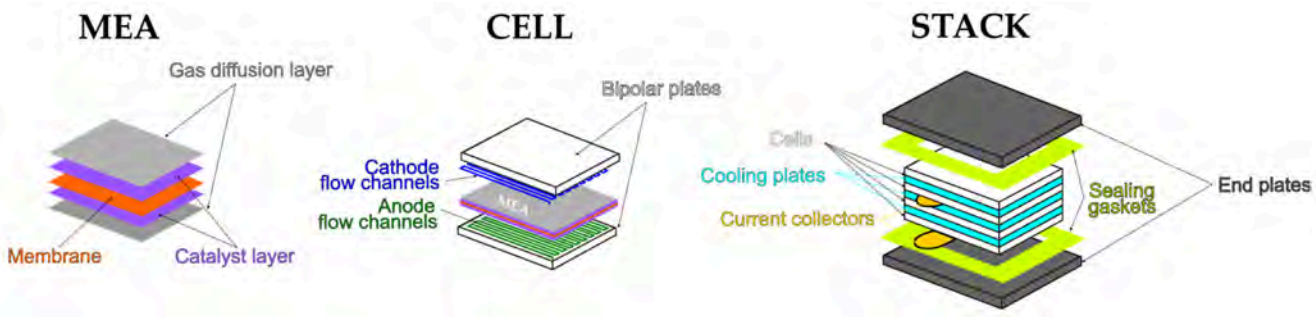

Figure 1. Structure of a PEM fuel cell [13].

To make the conversion of hydrogen energy possible, it is necessary to provide the reactants, keep the working temperature within optimal values by an appropriate cooling system, and control the voltage with an electric power control system. The correct humidification of the membrane is also a critical aspect and may require a separate water management circuit [14]. All of these sub-systems form the so-called Balance Of Plant (BOP) [12] and absorb parasitic electric power from the stack during normal operation and from a battery at start-up. Moreover, they affect the dynamic response of the fuel cell to variable loads.

The typical BOP of a self-humidified open-cathode fuel cell is shown in Figure 2. The inflow of air is guaranteed by the usage of one or more fans whose motors receive power from the stack, except for the start-up process, where a battery is used. The temperature of the stack is regulated by controlling the speed of the fan motors and, therefore, the mass flow rate of the fan. No external humidification is required because additives are incorporated into the catalyst layer or in the membrane to retain the water generated by reaction (1) [15].

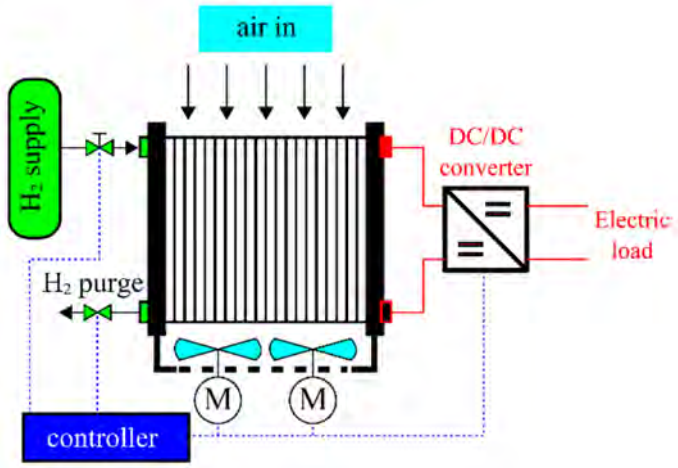

Figure 2. Balance of plant of a self-humidified open-cathode PEMFC.

Some commercial fuel cells adopt the short-circuit method to increase the proton conductivity of the proton exchange membrane by enhancing water production. A momentary short circuit induces an overcurrent in the fuel cell, which significantly increases the hydrogen–oxygen reaction rate, leading to more water formation. Moreover, it can also improve the activity of the catalyst by the removal of the oxides formed on platinum as a consequence of the slow oxygen diffusion kinetics on the cathode side [16]. Such techniques, relying on dedicated electronic control (the Short Circuit Unit or SCU) and typically developed by system integrators or fuel cell manufacturers, are often implemented without a thorough comprehension of the underlying mechanisms and the associated secondary effects. According to some authors [17], the application of short circuits accelerates performance degradation. The SCU can also harm the consumption of hydrogen, which was found to significantly increase, especially at low load [18]. However, insufficient studies are as yet available on this issue [19], in particular for open-cathode fuel cells, where the working temperature of the stack is also affected by the short-circuiting as found in this investigation.

The BOP also includes the hydrogen circuit and the electronic controller. Hydrogen is supplied from a tank that can be of three types: pressurized vessels, cryogenic tanks, or metal-hydride storage systems. The flow rate and the pressure of hydrogen are controlled using a regulation valve. The anode is usually dead-end, with a purge valve that is opened with a certain frequency to eliminate water accumulated at the anode because of back diffusion from the cathode and impurities [20]. The pressure difference between the inside and outside of the anode during the purge generates a loss of hydrogen flow, which removes accumulated water, restoring PEMFC performance and preventing deep voltage drops. The theoretical relationship between water content and ionic resistance in the membrane justifies using voltage as a practical indicator of hydration state. Purge frequency and duration are to be optimized to keep cell voltage drops below 100 mV to ensure the correct control of water [21] and minimize the consumption of hydrogen [22]. Bradley et al. [23] pointed out that the purge action penalizes the overall efficiency of the powertrain at part load.

Since the voltage of the stack decreases with increasing current (i.e., load) and is affected by the purge operation, a DC/DC converter is usually adopted to obtain the voltage required by the electric motor(s) for the propulsion of the vehicle. Fuel cells provide steady power but have a slower transient response due to fuel/air flow, reaction kinetics, and thermal management. Moreover, rapid current or power fluctuations cause degradation in fuel cells. On the contrary, batteries and supercapacitors can react quickly and can handle the fast load changes required, for example, by a UAV [24–27]. Therefore, a battery or a superca-

pacitor is added to the fuel cell power system to smooth down the dynamic variation in the fuel cell current and improve its lifespan. These secondary energy storage systems can be connected through DC/DC converters, thus obtaining active or semiactive configurations. In case of active configurations, several energy management strategies can be implemented to minimize fuel consumption, extend the vehicle endurance [24], and save the fuel cell life by regulating the current rate of change. However, to simplify the architecture and minimize the cost, a passive configuration is adopted in this investigation [26].

Rapid variations in load and elevation during the flight have a great impact on the performance of PEMFCs for aeronautical applications [13,28]. A rise in flight altitude determines a reduction in air temperature, density, etc., that affects the behavior of the fan. A sudden increase in the load accelerates the electrochemical reaction and increases hydrogen consumption without a simultaneous increase in the air flow rate due to the time lag of the BOP. This can cause rapid growth of the stack temperature and starving processes that can damage the membrane and reduce the performance of the PEMFC [29]. With a specific application to unmanned air vehicles (UAVs), the results of Atkinson et al. [30] indicated that PEMFC can be operated over wide ranges of temperature, relative humidity, airspeed, and elevation. However, a significant reduction in the maximum power of the fuel cell is observed during the flight due to increasing ambient humidity (up to 24%), flight speed (up to 28%), and elevation (up to 20%). Therefore, a further critical issue arises in the evaluation of fuel cell system performance in the case of application to aerial vehicles.

1.1. Goal, Novelty Claim and Contribution to the State of the Art

The goal of the present investigation is to analyze how dynamic mission profiles affect hydrogen consumption and system-level efficiency in an open-cathode PEMFC and to propose an energy-based assessment framework that includes balance-of-plant contributions and purge losses to improve the estimation of endurance in small vehicles equipped with this kind of propulsion system, like UAVs and light ground vehicles.

Most works in the scientific literature on fuel cells focus either on very small systems, such as single cells [31], or on powerful liquid-cooled stacks exceeding 10 kW. In the first case, the stack operates under controlled conditions without a cooling system [32]. In contrast, liquid-cooled stacks involve a more complex balance of plant (BOP) than considered in this investigation, typically requiring a dedicated cooling system, a closed cathode circuit, and a blower or compressor.

Studies on the sizing and management of open-cathode fuel cells for UAVs are usually based on experimental data obtained under quasi-stationary conditions (Tian et al., 2024 [33]; Liu et al., 2025 [34], He et al. [8]). Other investigations address dynamic tests aimed at modeling or controlling specific phenomena, such as stack temperature or purging frequency and duration [35]. For example, Hou et al. [36] observed that a step decrease in current demand causes the stack voltage to increase abruptly before gradually decreasing to the steady-state value; they proposed a logarithmic transfer function to predict voltage behavior during purging. Similarly, Tang et al. [37] analyzed the dynamic behavior of an externally humidified fuel cell stack under varying load profiles, investigating the effects on voltage, temperature, and flow rate.

A few studies have employed real UAV flight data. Santos et al. [27], for instance, analyzed current and voltage trends of the fuel cell and a secondary battery system, but did not consider the role of the BOP. Marqués et al. [38] calculated hydrogen consumption based on reaction stoichiometry, without accounting for additional consumption due to unsteady temperature conditions or hydrogen losses during purging. A similar approach is used by Figueroa-Santos et al. [4] in the optimization of the energy management of a fuel cell hybrid powered robot.

Other recent works have focused on PEM fuel cells for UAV applications under simplified operating conditions. Meng et al. [39] proposed a zero-dimensional model of a 3 kW air-cooled stack with metallic bipolar plates, validated against laboratory data, and highlighted a significant reduction in peak power with increasing altitude. However, their analysis was limited to simulated profiles without actual UAV flight data. Zine et al. [40] experimentally assessed an open-cathode PEMFC under altitude chamber conditions, showing net power losses at higher elevations, but only under steady-state operation, without accounting for transient load and BOP dynamics. Ferreira et al. [41] developed and tested a small PEMFC stack for UAVs under various ambient conditions, reporting efficiencies up to 52% at low current densities, but did not investigate realistic transient flight missions.

The main research question addressed in this work is related to the effects of realistic dynamic mission profiles on hydrogen consumption, efficiency, and overall performance of an open-cathode PEMFC system. To answer this question, a comprehensive experimental investigation was conducted on a 1 kW open-cathode PEMFC system equipped with its balance of plant and a passive supercapacitor buffer and operated under a representative UAV flight power profile.

Although previous studies have investigated open-cathode PEMFC systems for UAV and small mobility applications using experimental data and, in some cases, representative mission profiles [24,27], the combined impact of purge-related hydrogen losses, cooling-system parasitic consumption, and transient operating conditions on system-level efficiency and endurance has received limited attention.

The novelty of this work lies in the adoption of a holistic energy-based methodology that explicitly accounts for hydrogen losses due to purging, parasitic power consumption of the cooling system, and transient interactions among the fuel-cell stack, balance of plant, and supercapacitor. To the authors' knowledge, few experimental studies have simultaneously considered these dynamic penalties under realistic operating conditions, and none were found that combine them within the energy-based assessment framework proposed here.

The scientific contribution of the present work is the adoption of a comprehensive energy-based assessment framework that explicitly accounts for these factors under realistic operating conditions. The outcomes of this study can also support the development of both physics-based [42] and data-driven [43] models, as well as the implementation of advanced control strategies for key components—such as fans, purge valves, and the SCU—in vehicles equipped with open-cathode fuel cells.

1.2. Organization of the Paper

The paper is organized as follows. Section 2 describes the experimental setup, while the design of experiments is introduced and explained in Section 3. Section 4 presents and discusses the results. Section 5 introduces the proposed energy-based metrics for fuel consumption and efficiency during the vehicle mission. The results are summarized in conclusion Section 6, where the limitations of the proposed investigation are also discussed.

2. Experimental Setup

Experimental data acquired on the Dronebase eXplorer 1000, a tactical drone designed and manufactured by DroneBase S.r.l., Rimini, Italy, were used as a reference for analyzing a fuel cell system (FCS) under ground-based conditions replicating flight power demand. The authors selected an UAV as the reference application, as it represents one of the most relevant use cases for open-circuit fuel cells. However, the analysis proposed here can be extended to other kinds of low-power vehicles, for example ground robots [4].

The UAV is equipped with two Lithium-polymer batteries with the following nominal values: Capacity 22 Ah, 22.2 V, 10 C, max power 4.9 kW. The database includes data acquired with a frequency of 10 Hz on a mission with a maximum altitude of 168 m, with a flight time of about 16 min, of the following signals of relevance for this project:

- GPS: latitude, longitude, altitude.
- Battery current and voltage.

Figure 3 shows the data of battery power and flight altitude acquired on board. A Fast Fourier Transform (FFT) analysis was performed on the complete UAV mission profile to identify the frequency ranges containing the dominant power demand dynamics. The resulting spectrum revealed that most of the signal energy was concentrated at low frequencies, corresponding to the gradual variations in propulsion power associated with the flight phases. Conversely, the spectral amplitudes above approximately 0.2 Hz were found to be nearly constant and significantly lower than the dominant components, indicating the presence of broadband instrumental noise rather than actual power demand variations. Based on this observation, a low-pass filtering procedure was applied to remove the high-frequency components above 0.2 Hz while preserving the relevant low-frequency content of the mission profile. This filtering operation reduced the influence of measurement uncertainty and sensor noise without altering the overall energy content or the characteristic temporal evolution of the power demand. Note that the selected cut-off frequency corresponds to a period of 5 s, which is significantly shorter than the characteristic time scales of the UAV mission and of the fuel-cell thermal dynamics, as shown later in the manuscript. As a result, the processed signal more accurately represents the load variations experienced by the propulsion system and provides a reliable input for the subsequent experimental analysis of the fuel cell system.

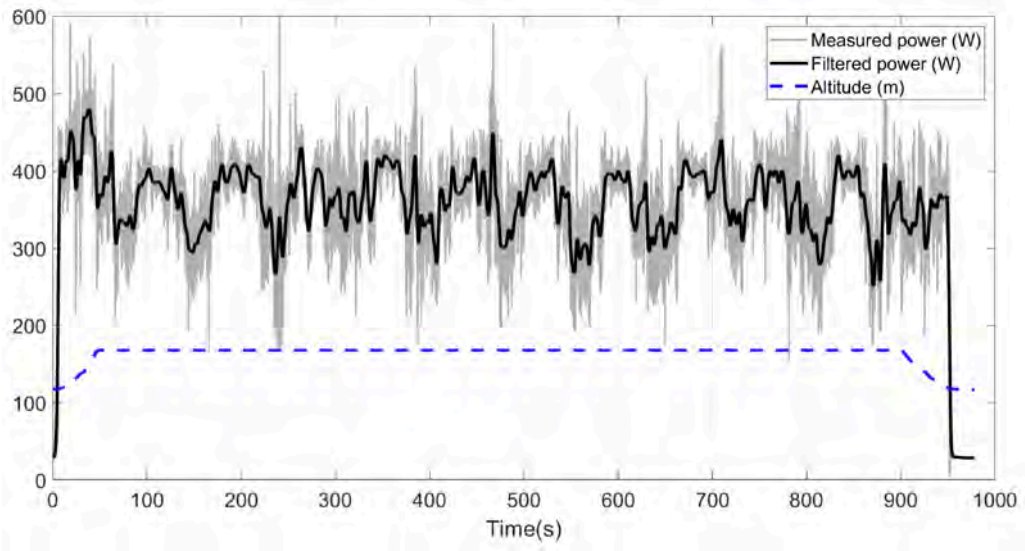

Figure 3. Power and altitude profiles of the reference mission.

A 1 kW FCS originally acquired for an ultralight prototype [3] was used for the analysis, being able to supply the required power in its high-efficiency region. An experimental setup was implemented to acquire all required data. The FCS includes four fans, an ultracapacitor (UC), a start-up battery, a purge valve, and a hydrogen regulator. The main specifications of the fuel cell system are reported in Table 1.

Table 1. Main specifications of the fuel cell system.

Category	Value
Type of fuel cell	PEM
Number of cells	50
Peak power	1100 W
Rated current	0–33.5 A @30 V
DC voltage	25–48 V
H_2 purity	99.99%
H_2 relative pressure	0.5–0.65 bar
Hydrogen consumption @ 1000 W	1.125 g/min
External temperature	5–35 °C
Max stack temperature	65 °C
Humidification	Self-humidified
Relative humidity	10–95%
Air cooling	4 × fan 80X25MM 13.8VDC
Start-up battery	Lead acid 12 V

Ultracapacitors or supercapacitors are electrochemical devices with much higher capacitance than conventional capacitors, thanks to their large electrode surface area and thin dielectric layers. The ultracapacitor that complements the fuel cell here has a discharge capacitance of 1.25 F and a rated voltage of 56 V. The supercapacitor is connected in parallel with the stack, with a passive hybridization scheme, while the fan is powered by the cell through a DC-DC converter that steps down the voltage to 12 V. A lead-acid battery is used at start-up only to power the auxiliaries. Each fan has a rated airflow of 2.3 m^3/min at the rated speed of 5600 rpm and 13.8 V. The fuel cell manual contains plots of voltage, power, fuel consumption, and airflow requirement vs. current that will be used for the validation of the model under stationary conditions. The fuel cell is equipped with a Short Circuit Unit (SCU) that is set to short-circuit the negative and positive electrodes of the stack at 100 ms every 10 s.

The flow chart of the experimental setup is illustrated in Figure 4. The adopted flowmeter is based on the thermal measurement principle, i.e., the mass flow rate of hydrogen is indirectly obtained from measures of temperature by means of two temperature sensors positioned one before and one after the heating system. The variable electronic load allows different input signals of current, voltage, or power to be implemented in the tests. The acquisition system includes not only the main signals from the stack (current, voltage, and temperature) acquired through the stack serial port, but also the electrical signals to the fan and the supercapacitor, the fan speed, the ambient conditions of temperature, pressure, and humidity by means of an in-house data acquisition system composed by a Arduino Uno board. Finally, the hydrogen mass flow rate and its temperature are acquired by means of the flowmeter serial port. All sensors are integrated and synchronized by means of a computer. The list of measured data, together with the acquisition frequency and accuracy, is shown in Table 2.

All tests were performed under uncontrolled ambient conditions. However, the whole experimental setup is designed to be included in an altitude chamber designed for the analysis of the PEMFC system under simulated flight conditions up to 2000 m. However, such a facility is not yet available for the tests.

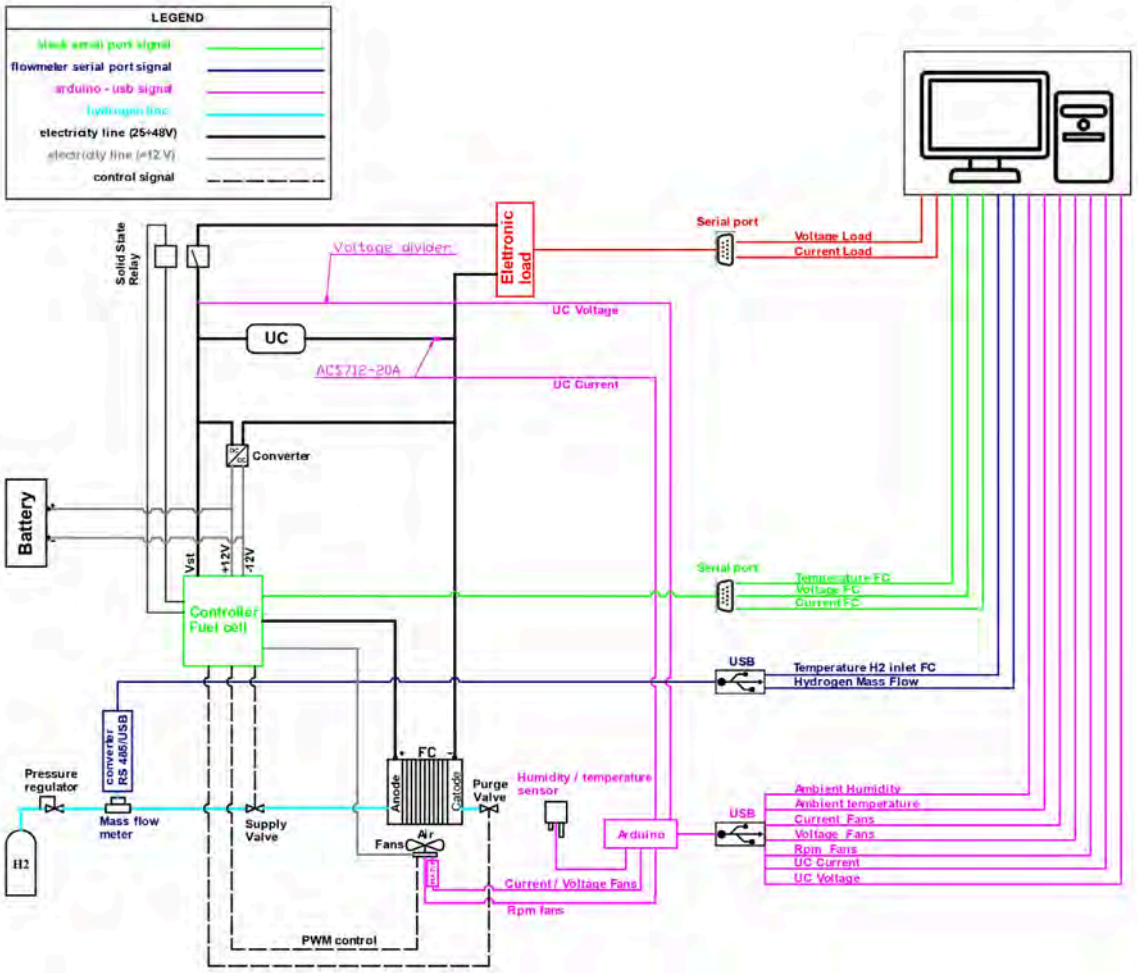

Figure 4. Flow chart of the experimental setup.

Table 2. Details of the experimental setup.

Measured Variable	Accuracy	Acquisition Frequency	Source
Stack Temperature	0.5 °C	1 Hz	Stack serial port
Stack Voltage	0.333 V	1 Hz	Stack serial port
Stack current	0.2 A	1 Hz	Stack serial port
Hydrogen Mass Flow	0.001 g/min	1 Hz	Flowmeter serial port
Temperature H2 inlet	0.1 °C	1 Hz	Flowmeter serial port
Voltage Fan (INA219)	3.9 mV	1 Hz	Arduino-USB
Current Fan (INA219)	0.05 mA	1 Hz	Arduino-USB
Fan speed	1 rpm	1 Hz	Arduino-USB
Voltage capacitor bank (voltage divider)	0.05 V	1 Hz	Arduino-USB
Current capacitor bank (ACS712-20A)	0.05 A	1 Hz	Arduino-USB
Humidity ambient	1%	1 Hz	Arduino-USB
Temperature ambient	0.1 °C	1 Hz	Arduino-USB
Load Voltage	0.01 V	1 Hz	Arduino-USB
Load current	0.01 A	1 Hz	Arduino-USB

3. Design of Experiments

The goal of the experiments is to analyze and quantify all the relevant parameters that define the dynamic behavior and the performance of the whole FCS. The input signals of the tests discussed in the present investigation are reported in Figure 5. The ambient values of temperature and Relative Humidity (RH) for each test, performed in the spring-summer period at Lecce, were recorded and reported in Figure 5 as well. The current and power signals refer to the system-level quantities, because the programmable load sets their values during operation.

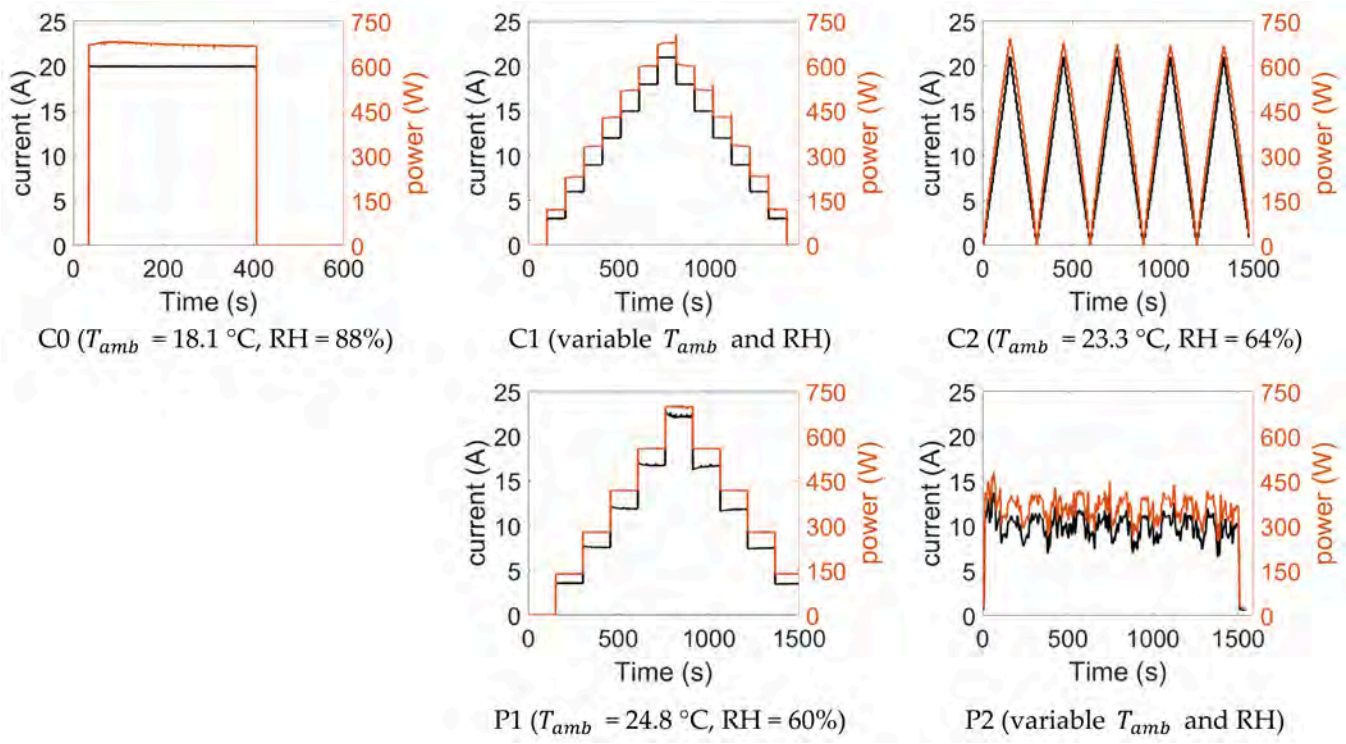

Figure 5. Input signals for the tests (set with the programmable load).

Test C0 is a square current signal with a step-up from 0 A to 20 A and then a step down from 20 A to 0 A after 400 s. The step input is traditionally used to characterize system dynamics because it produces a clear time-domain response from which important performance indices (rise time, settling time, overshoot, steady-state error) can be directly read [44].

In test C1, current was increased (and then decreased) with a step of 100 s to allow the stack to reach stationary conditions of temperature. This test was aimed at identifying the steady-state values of voltage, temperature, and other relevant parameters as a function of the load current input. To this scope, it was repeated nine times (C1.1–C1.9) and was performed with and without the activation of the SCU (C1.SCU).

The current was gradually increased and decreased with a triangular signal in test #C2. Therefore, the fuel cell stack is never allowed to reach the stationary conditions.

The second set of tests was obtained by controlling the load power. In the Test#P1, the power was increased and then decreased with steps of 100 s to reach stationary conditions as in test C1. Finally, in Test#P2, the power profile of Figure 3 was used as input to the system to study its behavior under ground-level reproductions of the flight. It was repeated six times (P2.1–P2.6).

All tests were performed with the stack at the ambient conditions to simulate "cold start", i.e., with the stack temperature starting from the ambient temperature. The time span of all tests, except C0, is 1500 s to match the duration of the recorded flight.

The experimental setup used in this investigation does not allow the control of ambient conditions, which has a strong effect on the performance of the FCS. For this reason, some tests were performed only once while tests C1 and P2 were repeated 9 and 6 times, respectively. Such repeated experiments were used to quantify variability through standard deviations and error bars.

Note that, due to the limited availability of hydrogen and the exploratory nature of the present experimental campaign, not all test conditions were repeated the same number of times. The primary objective of the repeated experiments (Tests C1 and P2) was to

quantify the variability of the fuel cell system response under representative steady-state and mission-like operating conditions, respectively. These tests were therefore selected for replication because they provide the most relevant information for assessing repeatability and for calculating standard deviations and error bars. In contrast, tests C0, C2, and P1 were mainly intended to characterize the qualitative dynamic behavior of the system and to identify trends in the transient response. Since these tests exhibited highly repeatable profiles and were not primarily used for statistical comparisons, a single execution was considered sufficient at this stage of the investigation. This strategy also reduced hydrogen consumption and experimental time, allowing resources to be allocated to a future testing campaign in an altitude chamber, where environmental conditions such as temperature, pressure, and humidity will be controlled. Moreover, a full inferential statistical analysis (e.g., *p*-values) was not included due to limited sample size and non-controlled conditions, and because the study aims at a physics-based, system-level characterization rather than hypothesis testing. A more rigorous testing procedure will be performed when the altitude chamber is available with the possibility to control ambient temperature, pressure and humidity.

4. Results and Discussion

Before analyzing the results of the tests, it is necessary to point out that some calibration issues were found with the flowmeter, as shown in Figure 6, where the raw measured signal for test C0 is reported together with the theoretical consumption of hydrogen $\dot{m}_{H_2,\,th}$ obtained from stack current I_{st} [12]:

$$\dot{m}_{H_2,\,th} = \frac{M_{H_2}}{2F} \cdot I_{st} \tag{2}$$

where M_{H_2} is the molar mass of hydrogen and F is the Faraday constant.

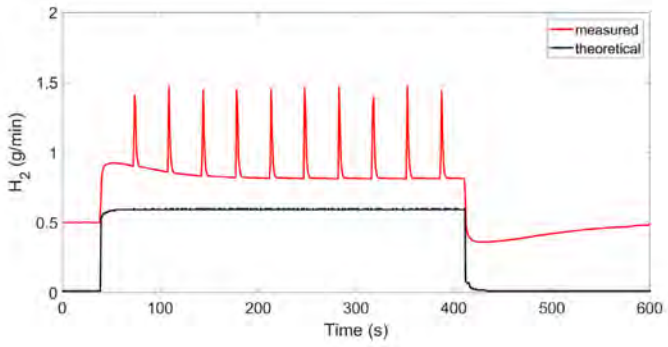

Figure 6. Measured vs. theoretical mass flow rate of hydrogen for test C0.

Note that the measured value is very high (about 0.5 g/min) also at no load, where the measured stack current is 0.4 A (to power the auxiliary) while the corresponding theoretical mass flow rate, from Equation (2), is 0.0126 g/min. The spikes in the measured mass flow rate are caused by the purge valve as discussed later.

Measuring hydrogen flow accurately is difficult due to its low density, high diffusivity, sensitivity to pressure/temperature changes, dynamic flow conditions, and the limitations of measurement devices. Proper calibration, fast-response meters, and careful system design are essential.

The problem with measured mass flow rate is obtained also in steady-state operation, as shown in Figure 7, where the steady-steady values of fuel consumption obtained with test C1 are reported, together with error bands showing the variability of the measured values. To reduce the effect of uncertainties and pressure regulator oscillations, the test was

repeated nine times. The standard deviation in the measurement of steady-state mass flow rate ranged between 0.02 g/min and 0.045 g/min, being, on average, about 5% over the 8 values of currents.

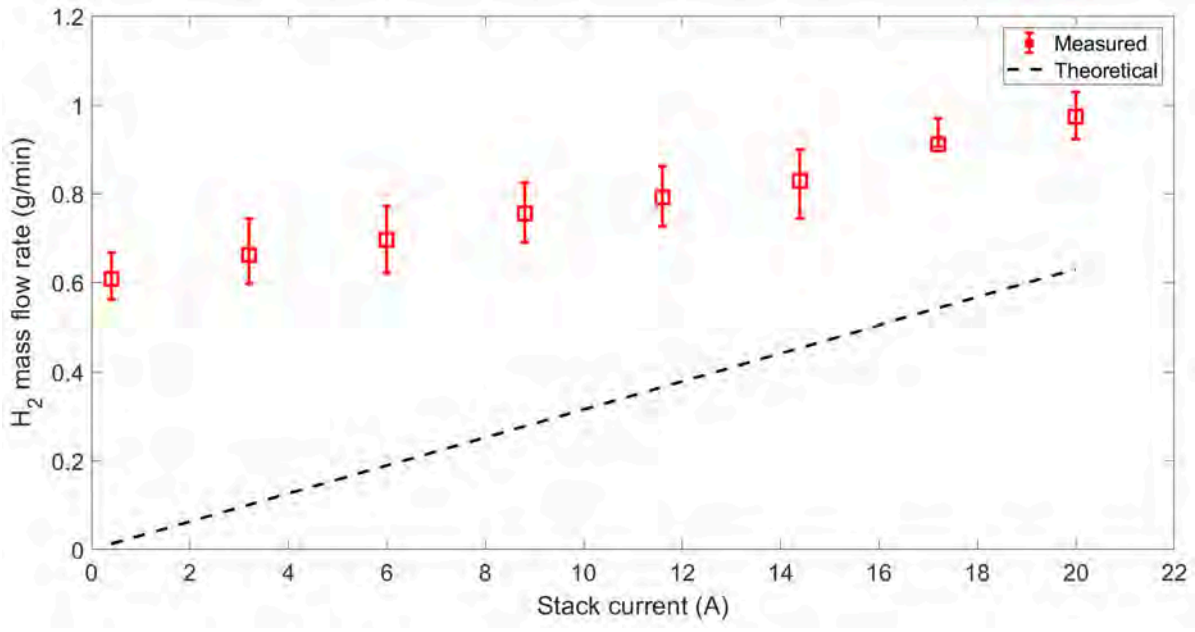

Figure 7. Steady-state fuel consumption vs. current: measured steady-state values compared to H_2 consumption from Equation (2).

Note that applying a constant offset to the measured values was not sufficient to obtain reasonable values of hydrogen mass flow rate and the dispersion in the values of steady-state hydrogen consumption is much higher than in the case of voltage and current.

After verifying the lack of losses of hydrogen in the whole hydrogen line and in the stack, the authors concluded that this could be caused by sensor degradation. While waiting for the replacement of the flowmeter, the mass flow rates measured in the present investigations were only used in qualitative terms.

4.1. Steady-State Operation

Test C1 was used to identify the steady-state operation by averaging the values of voltage, fan speed, mass flow rate, etc. at the end of each step up and down performed with the same level of current, after reaching a stationary value of stack temperature.

The steady-state polarization curve obtained with this procedure is compared to the data declared by the manufacturer in Figure 8. The manufacturer reports two polarization curves obtained at different values of temperature and humidity to show the variability of fuel cell performance with ambient operating conditions. The black error bars show the variability of the measured values in the nine tests performed with the same input profile, which is quite too low to be visualized except for the currents between 15 A and 20 A.

Under steady-state operation, there is no contribution of the UC to the power supply.

The four fans are used for cooling and for feeding the required oxygen. At start-up they are powered by the battery until the stack is able to generate a minimum current, found to be about 0.4 A, to power the fans at zero load.

The stack temperature under steady-state operation increases almost linearly with current as shown in Figure 9.

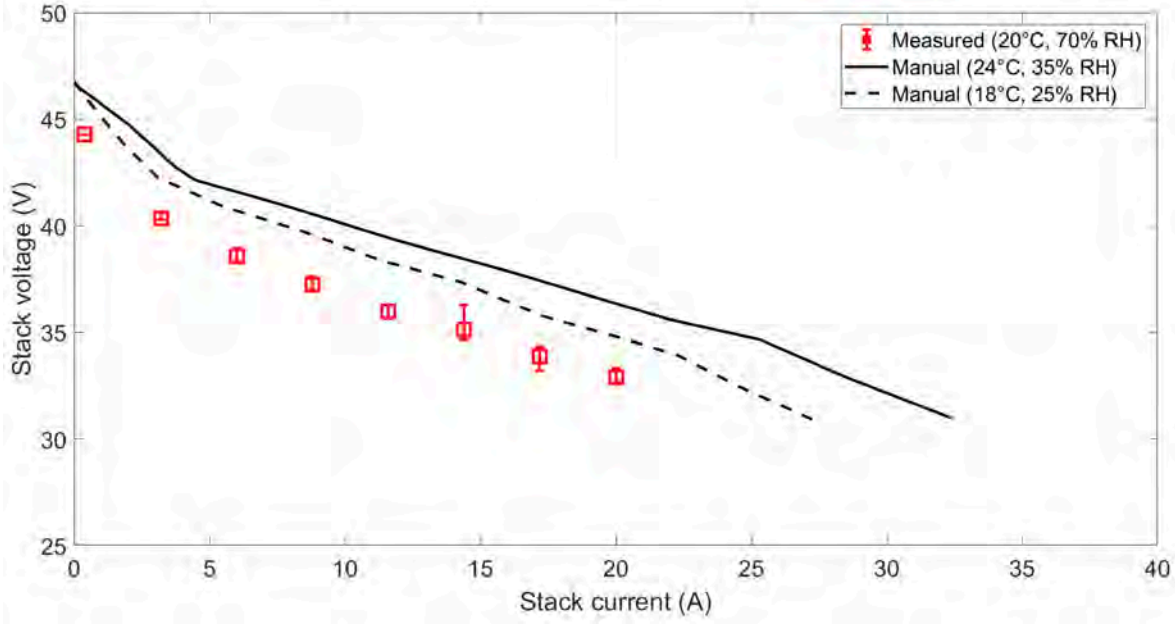

Figure 8. Estimated steady-state polarization curve, with error bars, plotted against manufacturer's data.

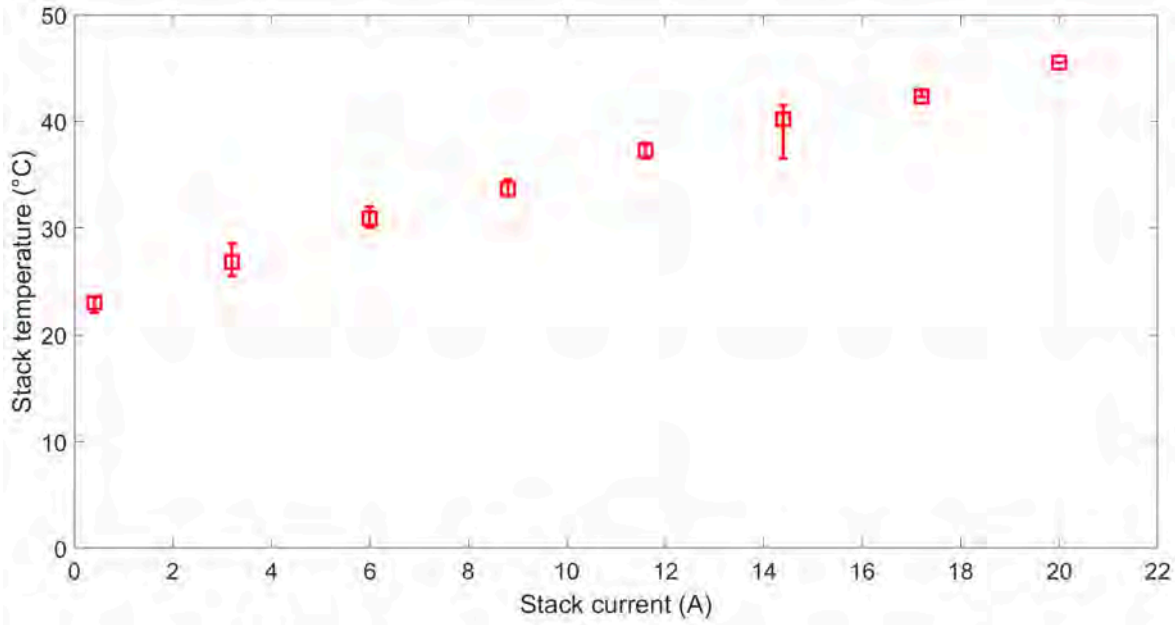

Figure 9. Steady-state values of stack temperature vs. stack current (with error bars).

Based on communication with the manufacturer, we found out that temperature is controlled by regulating the fan speed by means of a PWM on the basis of the stack current only. This kind of control is not quite suitable for a variable altitude application because it will lead to a decrease in the stack operating temperature with altitude, with a reduction in performance and efficiency.

The parasitic power of the fan increases in absolute terms with the load current as shown in Figure 10(left), but its relevance to the net power of the FCS decreases with load, being only 2% of the stack power for load currents higher than 12 A, see Figure 10(right).

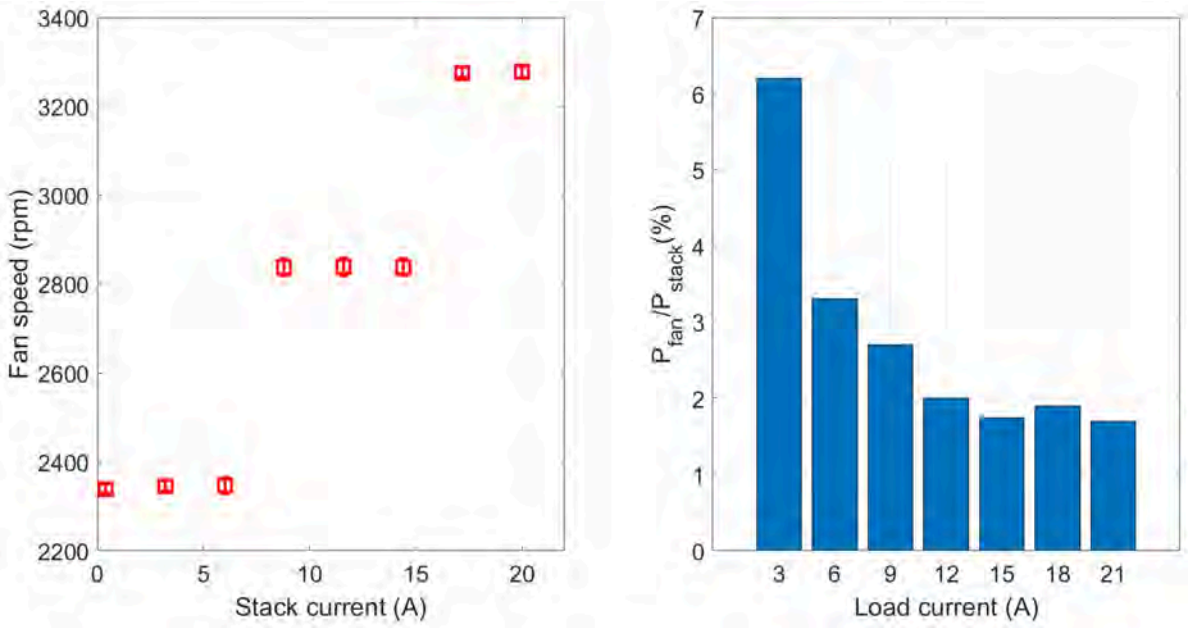

Figure 10. Fans behavior under steady-state operation vs. load current: fan speed with error bars (**left**), relevance of parasitic power (**right**).

The fan parasitic power, as expected, increases with rpm following a cubic law. The maximum parasitic power during test C1 is 11.2 W. However, under dynamic operations, larger values have been measured as discussed later.

4.2. Effect of the Short Circuit Unit (SCU)

The plots of Figure 11 compare the values of the stack signals measured on test C1 with and without the activation of the SCU. For the case without SCU, the nine repetitions are reported, together with the average (black line). The selected signals are stack voltage, temperature and power, and mass flow rate of hydrogen.

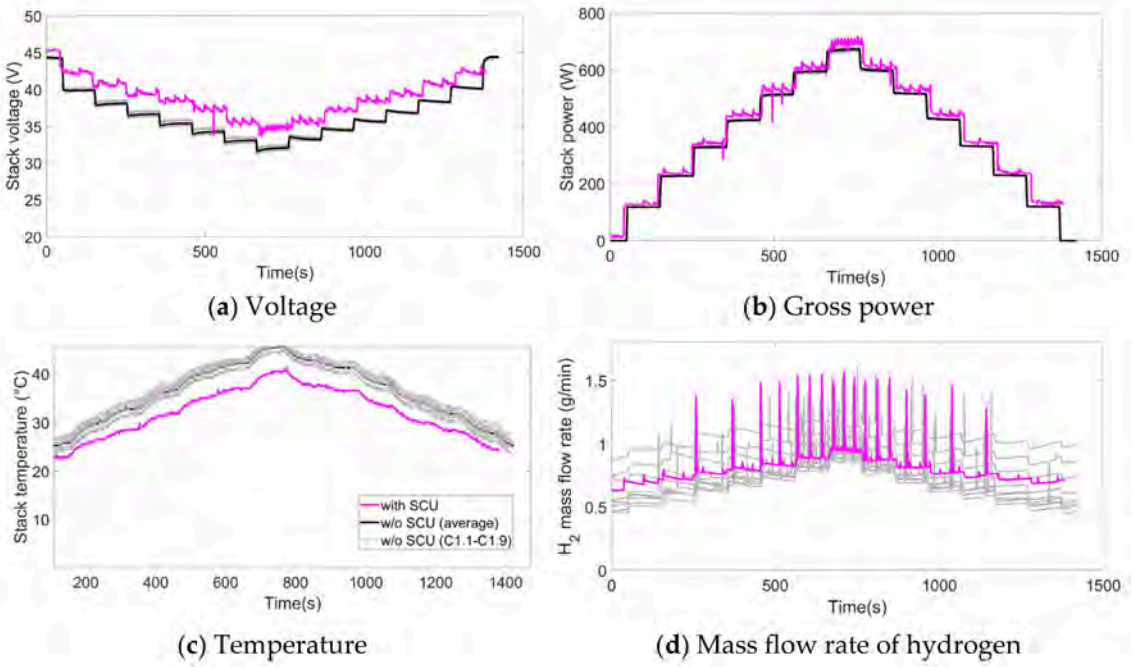

Figure 11. Effect of short circuit unit on the stack voltage, gross power, temperature, and hydrogen consumption (Test C1).

The behavior of the stack voltage vs. time without the SCU, Figure 11a, shows an undershot in correspondence to each current step, then a slow increase until the next current step when the current is increased. Similarly, an overshoot is present in correspondence of each step-down. Smaller perturbations of the voltage can be noticed at the opening of the purging valve. However, the voltage signal is quite regular, and the repeatability of the tests is very good, with small variation from test to test due to the slight differences in the ambient temperature. When the SCU is activated (magenta line), a noteworthy increase in the level of voltage and, consequently of power, Figure 11b, is obtained. The stack voltage is, on average, 1.94 V higher than in the case without SCU thanks to the better humidification of the cell. As a consequence, the stack power is also increased, particularly at high currents. On the other hand, the voltage and the power show a higher variability with time and current so that the cell never reaches a steady-state operating condition.

Figure 11c compares the levels of temperature, showing a higher dispersion, compared to the voltage, in the nine repetitions without SCU, caused by the uncontrolled ambient temperature. The temperature of the stack, however, is much lower in the case with SCU. To understand the behavior of the stack temperature, we can recall the thermal balance equation of the stack:

$$\dot{Q}_{gen} - \left(\dot{Q}_{nat} + \dot{Q}_{rad} + \dot{Q}_{fan} + \dot{Q}_{sens+lat}\right) = M_{st} \cdot C_{st} \cdot \frac{dT_{st}}{dt} \quad (3)$$

In this equation, T_{st}, M_{st}, C_{st} are the temperature, mass and thermal capacity of the stack, respectively. $\dot{Q}_{nat}$ is the heat flux dissipated by the fuel cell surface by means of natural convection with the external environment, $\dot{Q}_{fan} = \dot{m}_{air} c_{p,air}(T_{st} - T_{amb})$ is the contribution of the forced convection in the cathode side generated by the fan, and $\dot{Q}_{sens+lat}$ is the sensible and latent-heat-associated water warming and phase change. $\dot{Q}_{gen}$ is the heat produced from the exothermic chemical reaction and can be computed as $\dot{Q}_{gen} = (1.25 \cdot N - V_{st}) I_{st}$ [12].

Neglecting the other sources of heat transfer, Equation (3) can be written as $\dot{Q}_{gen} = \dot{m}_{air} c_{p,air}(T_{st} - T_{amb})$ at stationary conditions. Working with the SCU unit reduces the amount of heat released by the fuel cell, $\dot{Q}_{gen}$, because the improved humification reduces the ohmic losses of the cell. This explains the increase in voltage. On the other hand, the air mass flow rate is almost the same in the two cases because the fan speed is changed according to the current of the load.

The stack temperature has a relevant role in the efficiency of the stack [12]. The thermodynamic efficiency or maximum theoretical efficiency is defined as the ratio of the change in Gibbs free energy to the change in enthalpy. It decreases with temperature because of the increased contribution of entropy. The voltaic efficiency is defined as [12]

$$\eta_V = \frac{V_c}{1.25\ V} \quad (4)$$

where V_c is the cell voltage, $\frac{V_{st}}{N}$ with N number of cells in the stack, and 1.25 V the available electromotive force at standard operating conditions.

On the one hand, a higher temperature improves the thermodynamic efficiency and the reaction kinetics, reducing the activation losses. It also improves proton conductivity and helps evaporate excess water, limiting the accumulation of liquid in the cathode. On the other hand, excessive temperatures accelerate degradation mechanisms. In the case of SCU, the temperature is almost always below the minimum desired temperature which is 40 °C.

The results indicate that the activation of the SCU increases the average stack voltage at a given current, leading to an apparent improvement in voltaic efficiency. This behavior

can be attributed to the temporary enhancement of membrane hydration and catalyst activity induced by the short-circuit events, which reduce activation and ohmic losses. However, the higher stack voltage does not necessarily translate into an improvement in overall system efficiency. As shown by the temperature measurements, operation with the SCU results in a lower average stack temperature. This behavior may be attributed not only to the reduction in ohmic losses resulting from improved membrane hydration and proton conductivity, but also to the transient nature of the short-circuit events. During each short circuit, high-current pulses generate localized Joule heating and promote rapid water production within the membrane–electrode assembly [18]. Part of the generated heat is absorbed by the associated phase-change and water transport processes, while the intermittent character of the pulses limits sustained heat accumulation within the stack. As a consequence, despite the occurrence of localized heating phenomena, the average stack temperature remains lower than that observed during operation without the SCU.

The influence of the SCU on hydrogen consumption is evident in Figure 11d. Because purge events occurred at slightly different times in the nine repetitions, averaging the fuel-consumption traces without SCU would have produced misleading results; therefore, only the individual measurements are reported. The large peaks associated with purge operations are comparable in number and magnitude to those observed without SCU. However, additional fuel-consumption spikes appear during the short-circuit events. These spikes are particularly pronounced at low current levels, where the short-circuit current represents a larger increase relative to the nominal operating current. During each short-circuit event, the stack temporarily operates at very high current density, accelerating the electrochemical reaction rate and increasing hydrogen consumption. Since the electrical energy generated during these events is not fully delivered to the external load, the additional hydrogen consumed does not result in a proportional increase in useful output power, thereby reducing the overall fuel utilization efficiency. This observation is consistent with the findings reported in [18].

Therefore, although the SCU can improve voltage stability and mitigate some performance losses associated with membrane dehydration, its operation introduces an efficiency trade-off by increasing hydrogen consumption. A more detailed quantification of this trade-off, including the effects of altitude and ambient conditions, will be the subject of future investigations in the altitude chamber. Given the additional fuel consumption and the irregularities introduced in the power and fuel-flow measurements, the SCU was deactivated during the remaining tests to ensure a clearer assessment of the intrinsic dynamic behavior of the fuel cell system.

4.3. Measurement of the Dynamic Response

The results of test C0 were used to analyze and quantify the overall dynamic response of the whole fuel cell system, comprehensive of the ultracapacitor, purging valve and fan. The main signals for this test are shown in Figure 12.

From the plots of current, we can notice that the ultracapacitor smooth down the current demand to the fuel cell, with absolute peak values of about 2 A at the beginning and ending of the step signal. This effect is more evident in Figure 13, where the rates of change of load current and stack current are compared. Note the lower absolute value of rate of change of stack current in both the step-up and step-down.

Differently from what observed by [37], the stack voltage shows a small undershoot during step-up but no overshoot at step-down thanks to the role of the ultracapacitor. During the constant current operation, the stack voltage experiences no evident drops, but it undergoes a decrease after the undershoot because of the changes in the stack temperature.

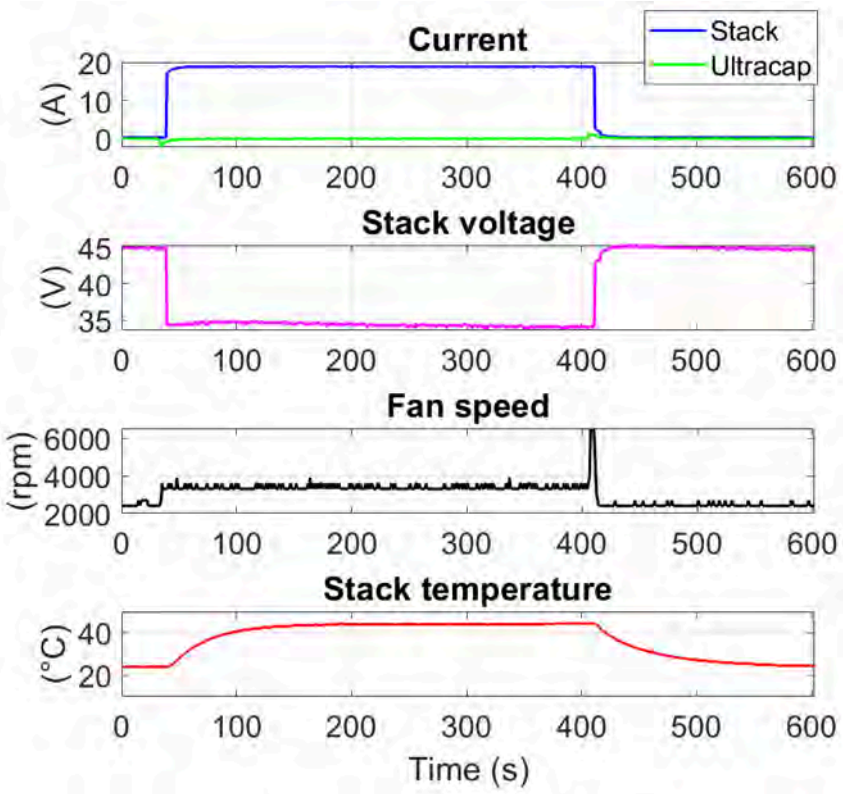

Figure 12. Results of Test C0 (T_{amb}= 21.8 °C, RH = 67%).

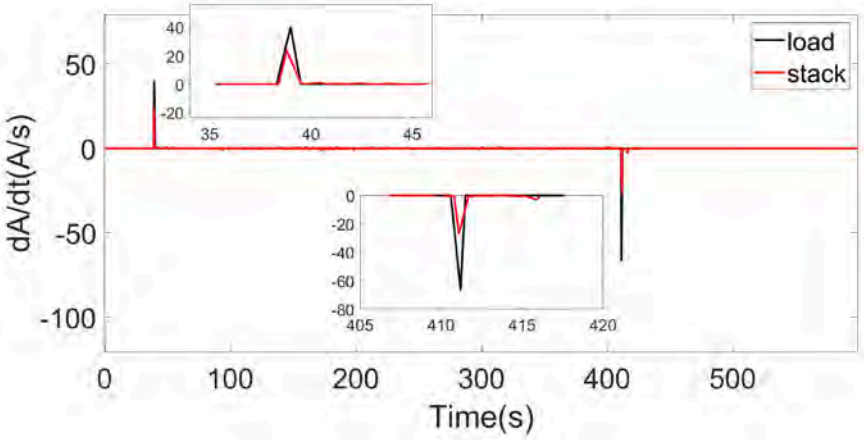

Figure 13. Current rate of change for load and stack (Test C0).

The fan speed has a very fast dynamic behavior, with a rise time of about 35 s. It reaches a peak of 6600 rpm at the beginning of step down where a fast decreasing of temperature is desired, proving that fan is not controlled based on temperature only in the case of dynamic load. This corresponds to a sudden increase in the parasitic power of the fan and, therefore, in a decrease in the net power of the FCS.

The thermal inertia of the fuel cell stack causes the temperature to increase slower with a rise time of 91 s and a settling time of 191 s. This delay in reaching the steady-state temperature affects the voltage and, therefore, the voltaic and the thermodynamic efficiency of the stack.

4.4. Temperature and Voltage Under Dynamic Operating Conditions

The rate of change of the current under the other tests is shown in Figure 14. Compared with C1, test C2 is characterized by a more regular rate of change since current is continuously increased and decreased. When the power is used as input instead of current, as in test P1, the rate of change of the current is higher because it is affected by the need to compensate for the changes in voltage with temperature. Very high rates of change are also obtained in test P2, showing that the ultracapacitor is not sufficient to smooth down the dynamic request of power to the stack.

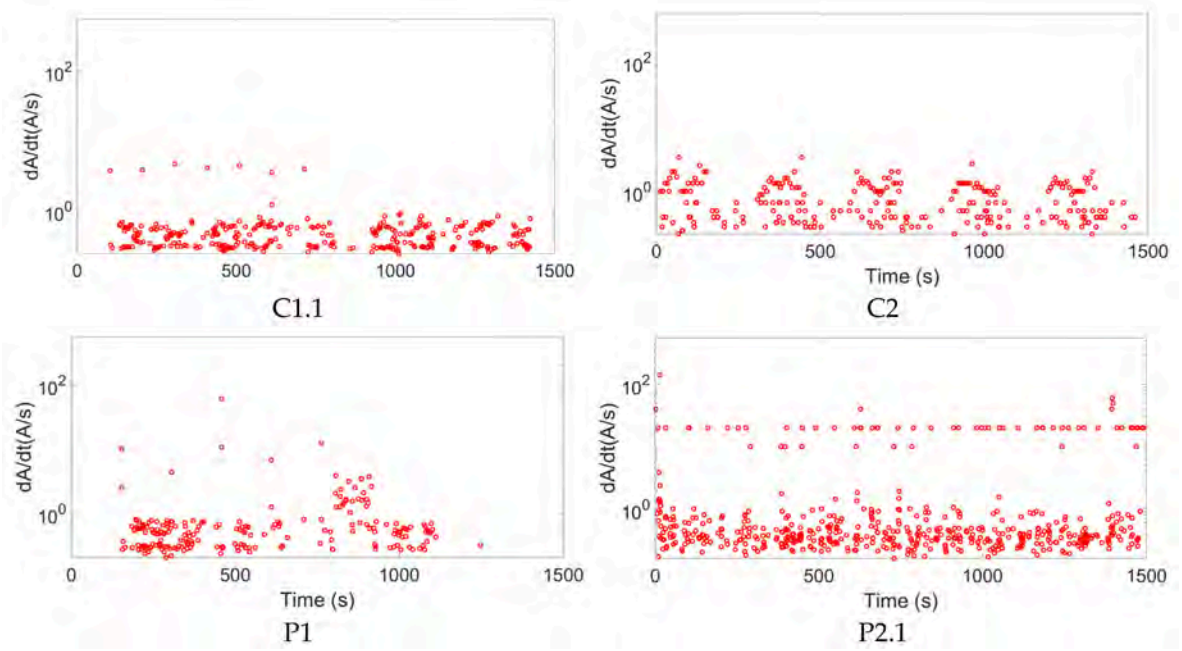

Figure 14. Rate of change of stack current in the dynamic tests.

Figure 15 compares the stack behavior—both temperature and polarization curve—under tests C1, C2, P1, and P2. The plots report the voltage and temperature measured during the transient tests, together with the steady-state curves (red line). A ±5% uncertainty bar is added to the steady-state curves to highlight the differences between steady-state and dynamic values. Filled and empty blue markers represent the values recorded during the increasing-current phase (Ist+) and the decreasing-current phase (Ist−), respectively.

In test C1, where the fuel cell is allowed to reach steady-state operation, the stack operating points cluster closely around the steady-state line in the left-hand plot. At each current level, the temperature is lower than the steady-state value during step-up transitions and higher during step-down transitions, reflecting the influence of the previous current level. The stack voltage follows these temperature variations, showing only small deviations from the steady-state curve.

In test C2, because the load current varies continuously, the temperature never reaches its steady-state value. A clear hysteresis appears: the temperature is consistently higher than the steady-state value when the current decreases (Ist−). Except during the cold-start phase, the temperature is also higher than the steady-state values for much of the increasing-current phase (Ist+). In terms of voltage, the highest values occur during the Ist− regions, again due to the higher temperature.

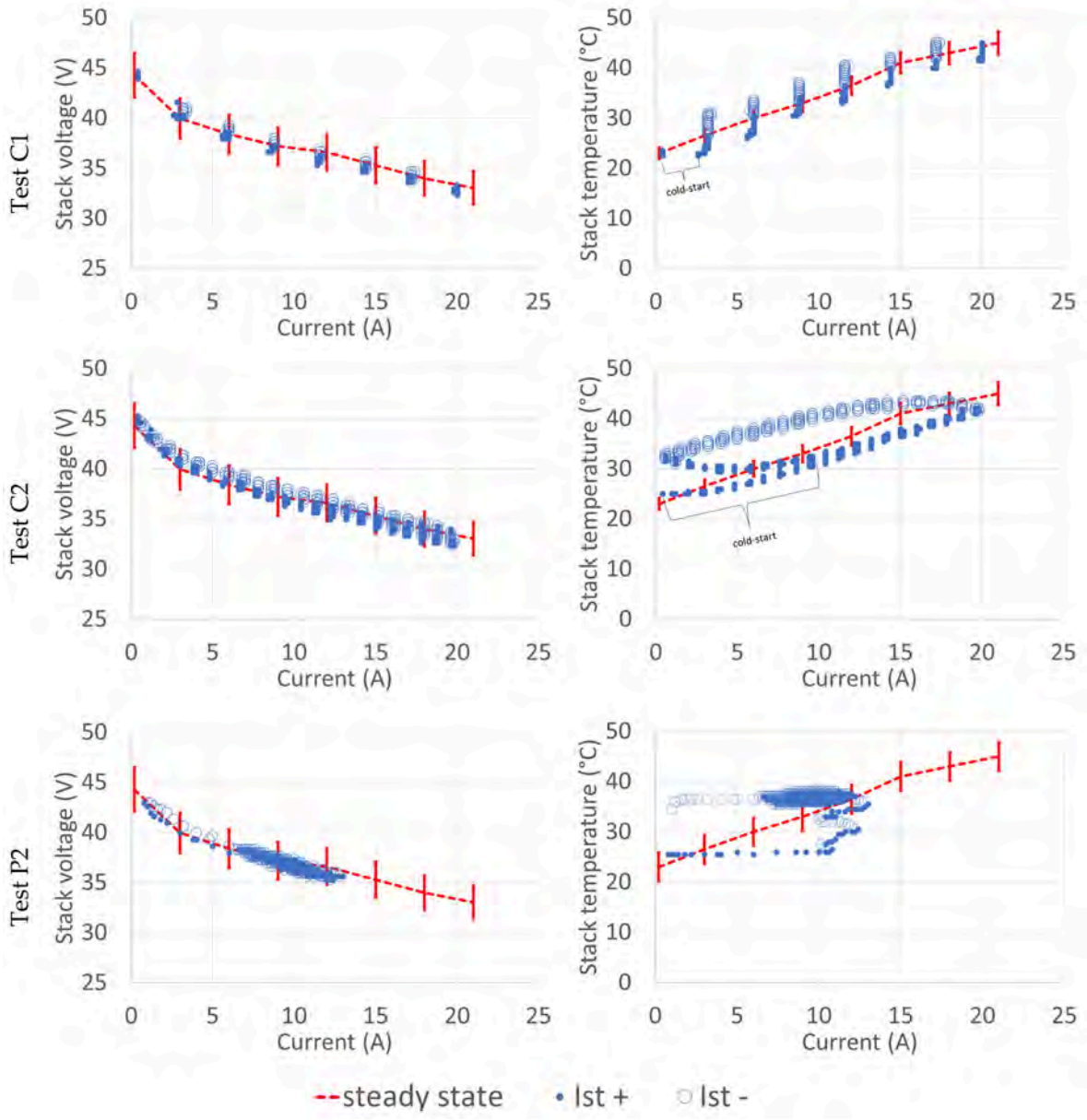

Figure 15. Effect of unsteady operation on stack temperature (**left**) and polarization curve (**right**). The red dotted line refers to the steady-state operation and shows an uncertainty bar of ±5%. The filled and empty circles represent the transient operation when current is increased or decreased, respectively.

The largest deviations from the steady-state temperatures occur during the test P2, where the temperature remains around 38 °C for most of the test and the voltage stays below the steady-state curve. Nevertheless, all voltage deviations remain within the ±5% uncertainty bar.

4.5. Hydrogen Flow Measurements and Purge-Related Phenomena

The measured hydrogen mass flow rate is shown in Figure 16 and compared with the theoretical consumption (black line) calculated from the stack current using Equation (2). The theoretical hydrogen consumption at zero load current is not null but equal to 0.013 g/min because of the parasitic power of the BOP. This implies that the observed discrepancy between theoretical and measured values cannot be attributed to the parasitic power of the auxiliary components, since the two curves should coincide, at least, at zero load current. At higher current levels, deviations from the theoretical value

are expected because of other phenomena such as small leaks, internal short circuits, or hydrogen crossover to the cathode.

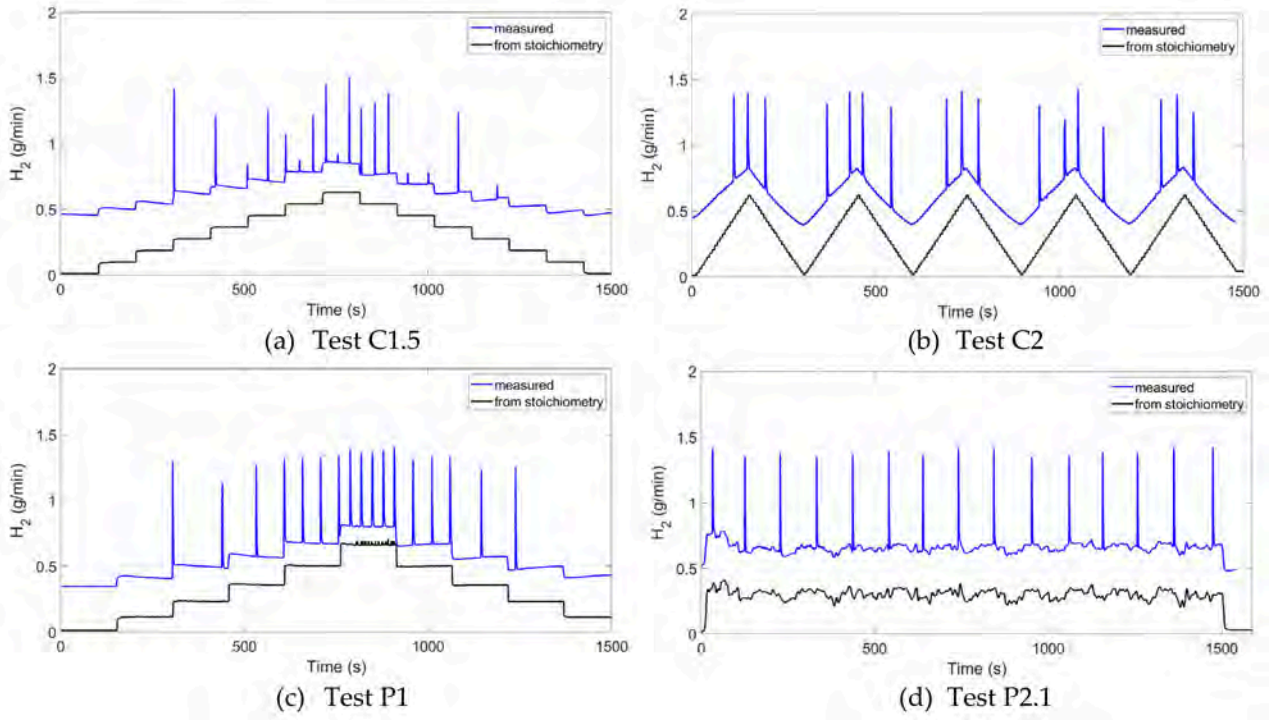

Figure 16. Measured mass flow rate of hydrogen plotted against stoichiometric values.

Furthermore, the measured hydrogen mass flow rate is not proportional to the stack current and exhibits overshoots and undershoots when the current is suddenly increased or decreased, respectively. However, a direct quantitative comparison between the measured and theoretical curves is not meaningful due to the limited repeatability of the tests and the previously discussed calibration issues affecting the flow meters. For this reason, the results reported in Figure 16 are used primarily to qualitatively highlight the dynamic effects of the system and, from a quantitative standpoint, to estimate the hydrogen losses associated with purge events.

The purge valve opening frequency can be identified by the spikes in the measured mass flow rate. According to the manufacturer, the opening frequency depends on the stack current while the opening time is constant. As a consequence, the height of the peaks of fuel consumption associated with each purging process is almost the same in all tests, being not affected by the current request or the dynamicity of the test. The losses of hydrogen, however, are larger when the current is increased because of the higher frequency of purging, as shown in Figure 17 which compares tests C0 and P2. However, some peaks are not fully captured by the available instrumentation, as shown in Figure 16a,b. In addition, a rigorous quantification of these losses is hindered by the lack of proper calibration of the flowmeter.

Figure 18 shows the recorded hydrogen mass flow rate $m_{H_2 in}$ for the six repetitions of test P2.

In conclusion, the tests highlight the critical challenges associated with accurately measuring hydrogen mass flow rate, as well as the need for a high-frequency data acquisition system to properly capture purge and SCU events. This could explain why it is quite impossible to find experimental studies on this kind of systems that reports the actual measurements of hydrogen flow rate with or without purge. For example, Strahl et al. [45]

proposes a similar approach to estimate the losses of hydrogen in purge but does not report the actual values obtained from the tests.

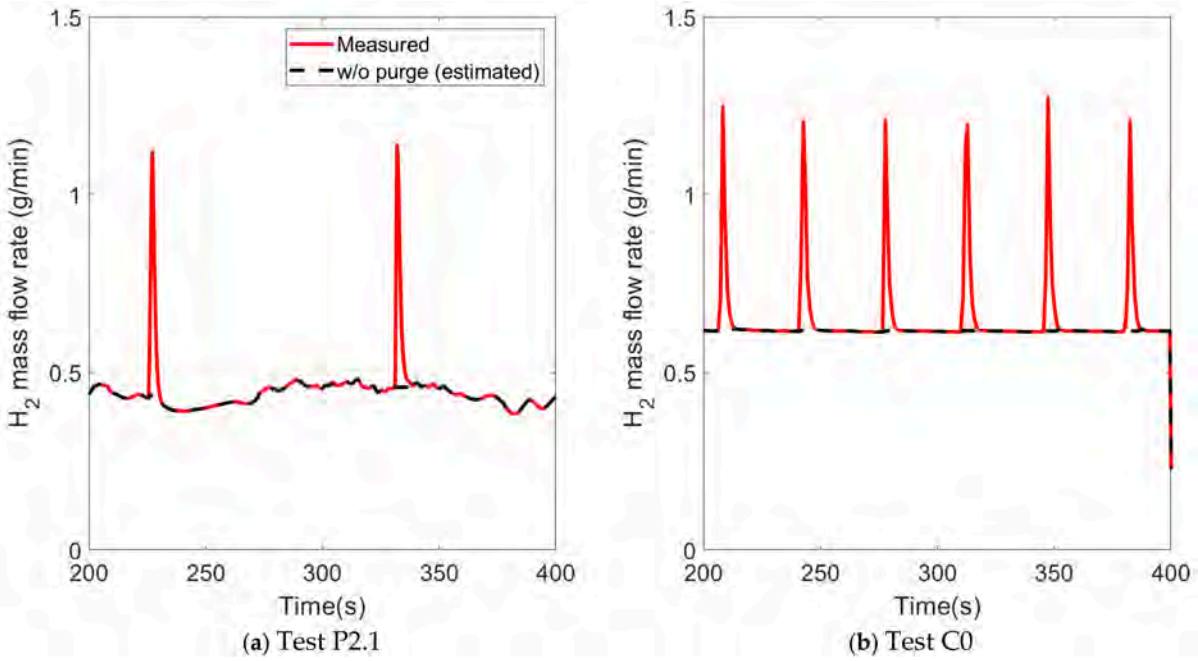

Figure 17. Estimated hydrogen consumption without purge (black line) vs. measured signal.

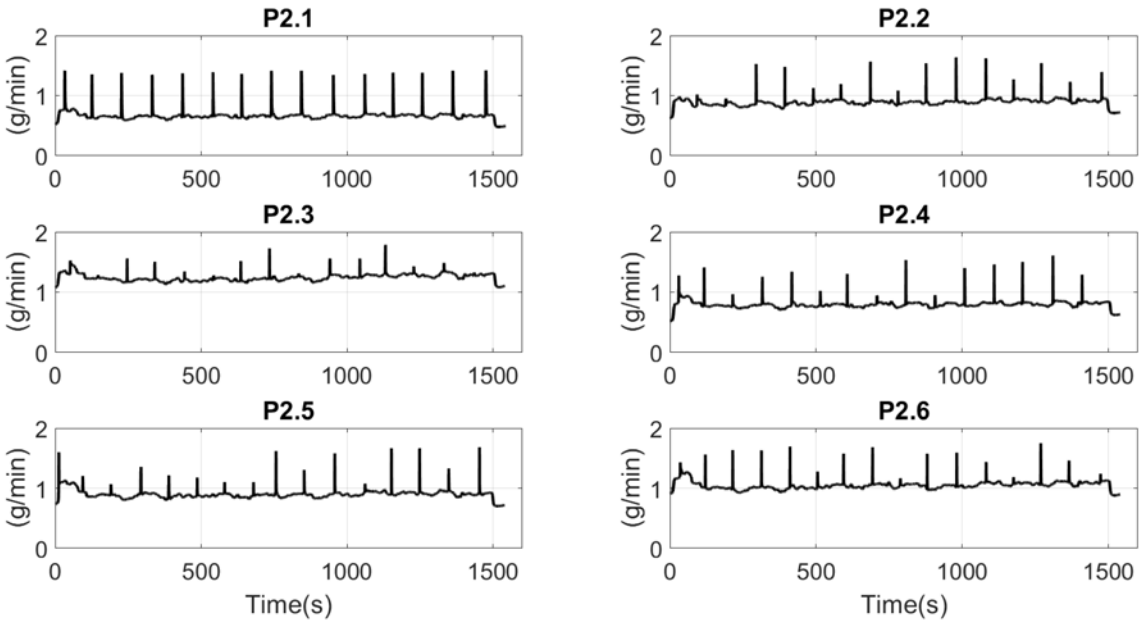

Figure 18. Recorded mass flow rate during the six repetitions of test P2.

4.6. Parasitic Power of Auxiliaries Under Dynamic Operation

The plots of Figure 19 depict the power of stack, UC, and fan over the five tests, including test C1 performed with the activation of the SCU.

The role of the ultracapacitor is to absorb the high-frequency component of the load power. The fuel cell stack and the UC share the same DC bus and, in steady-state, operate at the same voltage. When the load current suddenly increases, the stack voltage drops below the UC voltage; the UC then rapidly discharges until the voltages equalize. Conversely, when the stack voltage exceeds the UC voltage, the UC is charged. The UC charge/discharge process is fast but not instantaneous because it is affected by the internal

resistance of the cells and the interconnection circuit. Consequently, the current flowing into the UC depends both on its state of charge (through the voltage difference between stack and UC) and on the maximum current that the fuel cell can deliver at that instant.

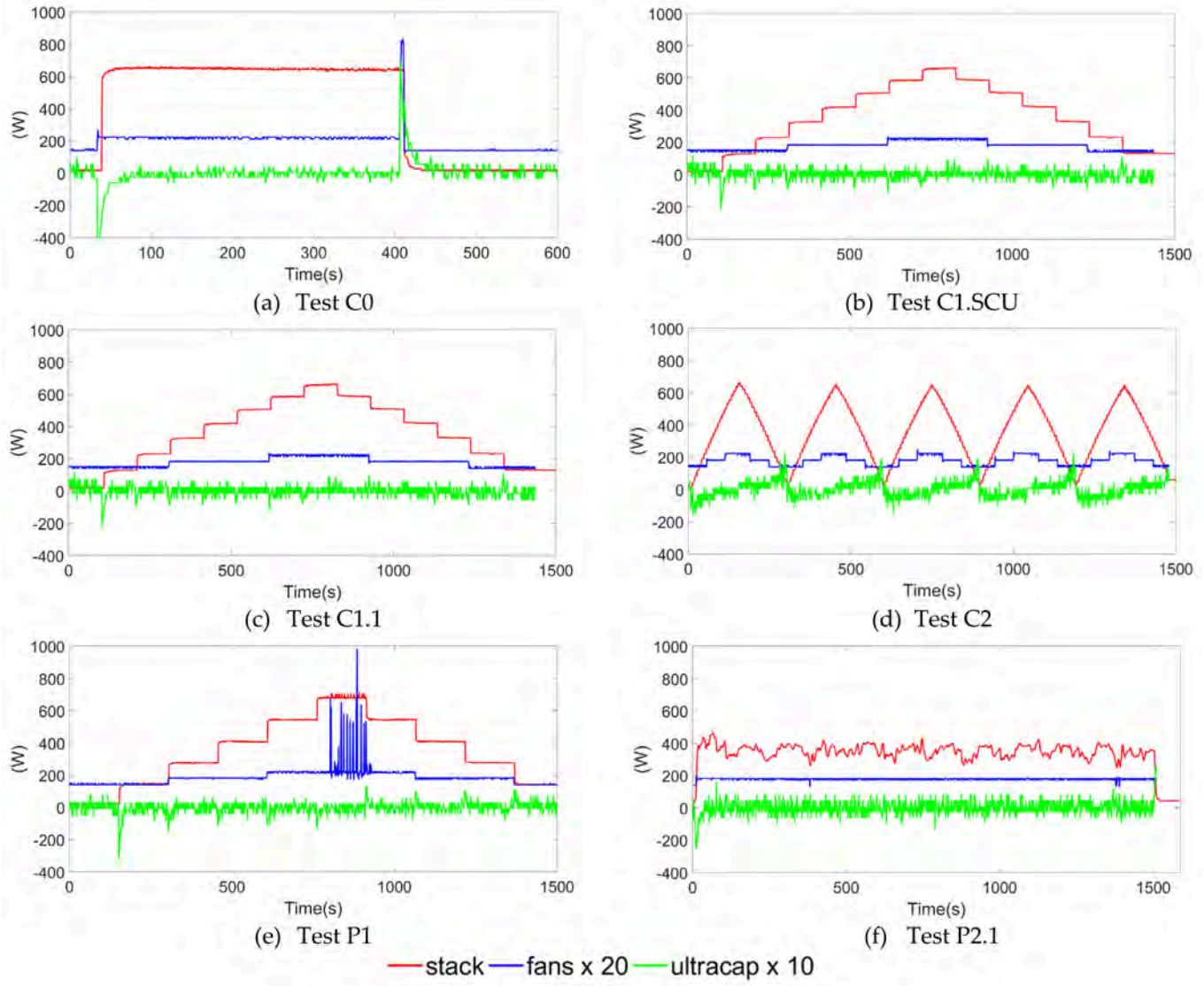

Figure 19. Parasitic power of the fans and contribution of the ultracapacitor.

In absolute terms, the UC contribution is the highest for test C0 where the peaks of about ±50 W at the step-up and step-down events were measured, because of the very high rate of change in current, while it is minimum for test C1 performed with the SCU off. When the SCU is activated, the UC must counteract the increase in voltage and the current caused by the short-circuits. Similarly, in the case of constant power request (P1) the UC must counteract the reduction of voltage and the increase of current caused by the accumulation of impurities between two consecutive purging events. This explains the presence of relevant intermediate peaks in both tests.

In the case of test C2, the UC contribution is also quite relevant because of the continuous variation of the load current calls for the need to compensate for the slow dynamics of the stack with the help of the ultracapacitor. This is particularly true when the current is brough to zero and then increased again. In the case of test P2, an undershot and an overshot are present only at the start and end of the mission, respectively.

The fan parasitic power is directly linked to the fan speed whose measured values are plotted in Figure 20, together with the steady-state values obtained by interpolating the

curve of Figure 10(left). Note that thermal inertia significantly affects the parasitic power of the auxiliaries, in particular when the current is suddenly decreased. In the case of test P1 the control of the fan speed becomes instable when the power request of the load exceeds 600 W. In fact, many spikes can be observed in the high-current zone of the blue signal of Figures 19e and 20c. This is another proof that the control system of the fans needs to be optimized.

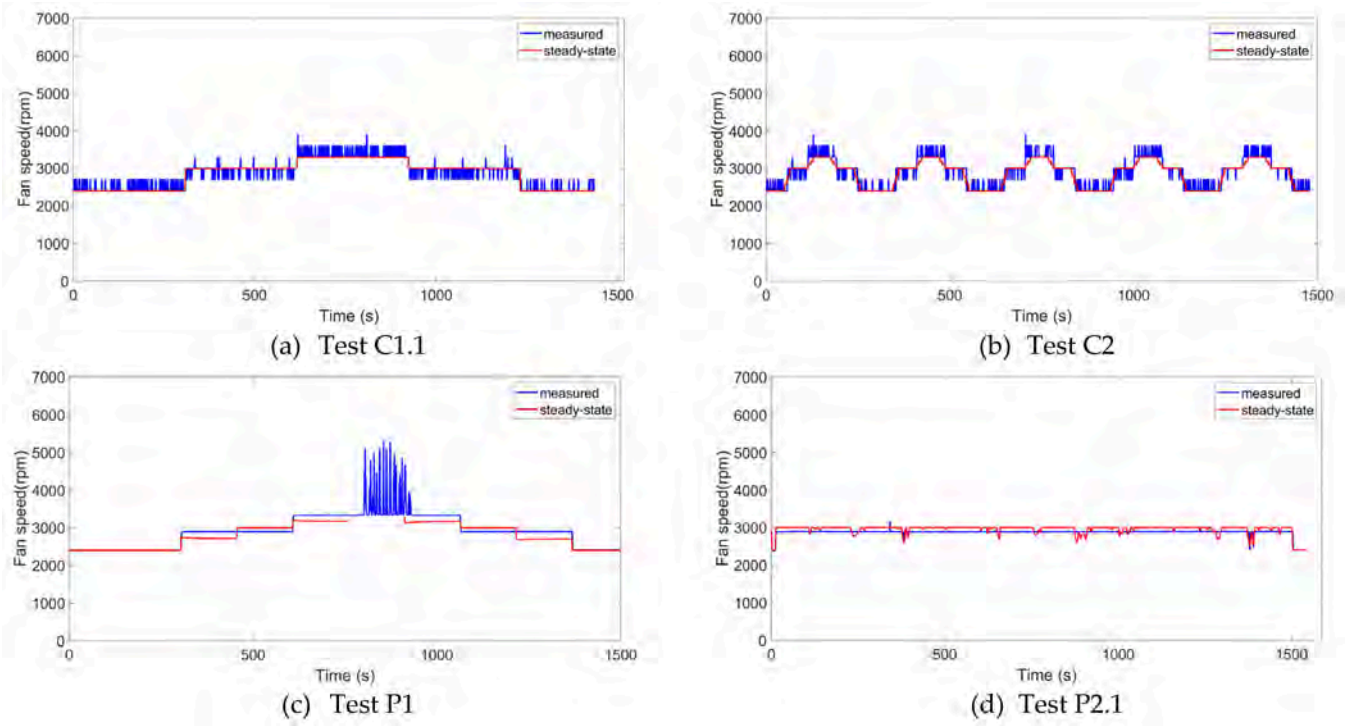

Figure 20. Measured fan speed plotted against steady-state values.

The instability of fan speed in the high-power region is an indication of the unsuitability of the present fan control strategy that set the desired temperature on the bases of current input only. More advanced control methods have been presented in the scientific literature [13], like the sliding mode [46], fuzzy logic [47], and model-predictive controllers [48]. They will be taken into consideration in the continuation of the project.

5. Energy-Based Metrics for Fuel Cell

The performances of fuel cells systems are usually analyzed by means of power-based metrics like voltaic efficiency and hydrogen mass flow rate is usually estimated directly from the current signal by using the stoichiometry of the reaction. The results of the present investigation have pointed out the limitations of such approach. For this reason energy-based metrics are here proposed and discussed.

Figure 21 shows the voltaic efficiency of the stack during the first 300 s of test P2, considered as a reference mission for the FCS, calculated using Equation (4) from the voltage data recorded in the six repetitions of the test.

The voltaic efficiency decreased with increasing current, as expected, but it is also influenced by stack temperature. The minimum value, equal to 54.3%, is observed in repetitions 4 and 5, which were performed at the lowest ambient temperature. Notably, a difference of only 2 °C in ambient temperature can lead to a variation of up to three percentage points (Test P2.2 vs. Test P2.5). Since the efficiency varies with time due to the dynamic input signal, an average value calculated over the entire test, hereafter denoted as $\overline{\eta}_v$, is used for the subsequent analysis.

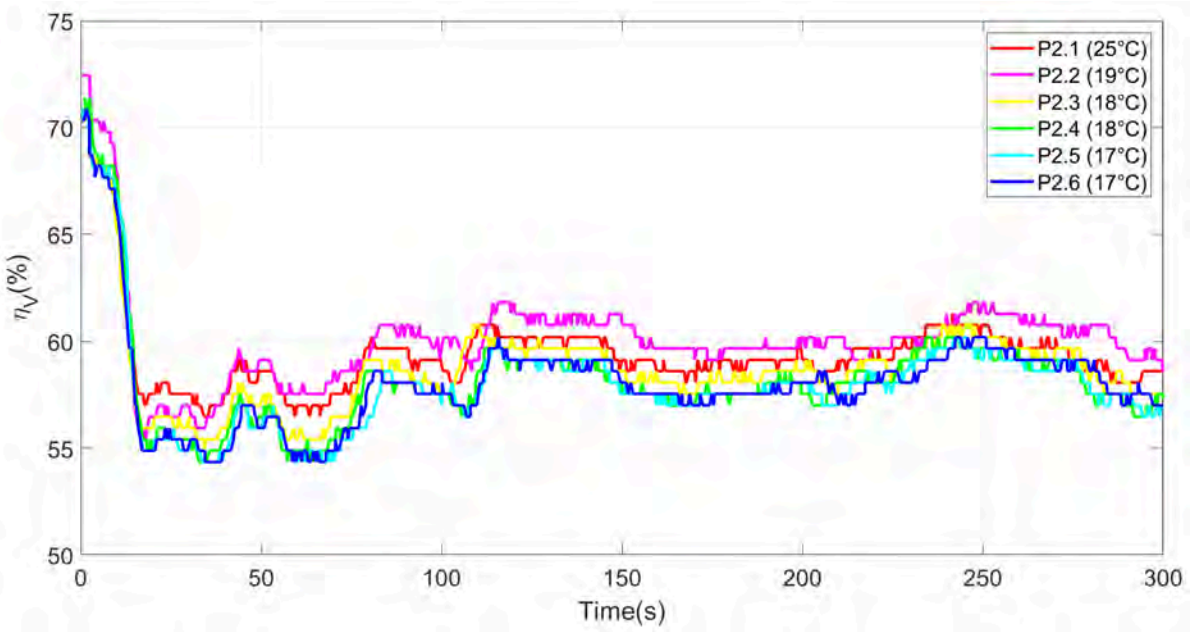

Figure 21. Voltaic efficiency of the stack during the first 300 s of test P2. Each curve represents one of the six repetitions; the ambient temperature is reported in round brackets.

The overall theoretical hydrogen consumption over the mission is then computed as

$$m_{H_2th} = \frac{M_{H_2}}{2F} \cdot \int_0^T I_{load} dt \tag{5}$$

where T is the mission duration. In this equation, the load current, I_{load}, is used instead of the stack current for two reasons. First, the stack current measurement exhibits lower accuracy. Second, from a methodological perspective, the load current represents the actual net current of the whole fuel cell system. Therefore, m_{H_2th} represents the hydrogen consumption obtained by neglecting parasitic power and purge losses, as commonly done in the scientific literature [40].

However, not all the hydrogen supplied to the stack reacts to produce electricity. To account for this, the fuel utilization factor μ_F is introduced. It is defined as the fraction of the supplied hydrogen that reacted and can be estimated as the ratio between theoretical and actual hydrogen consumption [4]. In global terms, it can be written as

$$\mu_F = \frac{m_{H_2th}}{m_{H_2in}} \tag{6}$$

where m_{H_2in} is the total hydrogen consumed during the test.

The following procedure is introduced here to obtain a conservative estimate of the total hydrogen consumption, $m^*_{H_2in}$:

$$m^*_{H_2in} = m_{H_2th} + m_{\text{purge}} + m_{\text{SCU}} \tag{7}$$

where m_{purge} is the hydrogen mass lost during purge events, that could be estimated as the difference between the cumulative measured hydrogen flow with and without the purge spikes (see Figure 17) over the entire test. Unfortunately, a quantitative analysis of the total hydrogen consumption is not possible with the current instrumentation. For steady-state operation values of 90–95% reported for the utilization factor in [49,50]. In case of SCU activation, an additional mass m_{SCU} penalizes the utilization factor and the poverall efficiency.

Transient effects and additional factors, such as small leaks, internal short circuits, or hydrogen crossover to the cathode, can further increase the discrepancy between theoretical and actual hydrogen consumption. For instance, Li et al. [51] reported a very low utilization factor of 39.6% during a flight test of a fuel-cell-powered UAV. Although this value is neither explained nor discussed by the authors, this analysis of the scientific literature confirms the need of a comprehensive energy-based approach.

The net power of the entire FCS can be expressed as follows:

$$P_{net} = V_{st} I_{st} + P_{UC} - P_{fan} - P_{par} \tag{8}$$

where V_s and I_s are the stack voltage and current, respectively; P_{fan} is the parasitic power of the cooling fan; P_{UC} is the contribution of the ultracapacitor; and P_{par} includes the parasitic power of the purge valve, control electronics, cable voltage drops, diode losses, and similar effects. In the FCS, P_{UC} is positive during charging and negative during discharging, while P_{par} is always positive. Although P_{par} could theoretically be obtained as the difference between measured quantities of load and stack power, its magnitude is extremely small and cannot be reliably quantified with the available measurements.

The ratio between net electrical power and chemical power defines the overall or net efficiency of the fuel cell system:

$$\eta_{net} = \frac{P_{net}}{\dot{m}_{H_{2,in}} LHV} \tag{9}$$

In this investigation, the net power coincides with the power measured at the load. However, the net efficiency cannot be calculated instantaneously because of purge and SCU losses. Therefore, an energy balance approach is more suitable.

The high repeatability of the tests, in terms of both power and energy, is confirmed by the low standard deviation observed not only for net energy but also for fan energy. As shown in Table 3, the fan parasitic energy accounts on average for 2.46% of the stack energy.

Table 3. Estimated energy flows during the mission (test P2).

Test	E_{net}	E_{fan}	E_{stack}	$\frac{E_{fan}}{E_{stack}}$ (%)
P2.1	150.56	3.75	154.15	2.43%
P2.2	158.38	4.05	162.04	2.50%
P2.3	155.24	3.88	158.77	2.45%
P2.4	153.44	3.84	156.88	2.45%
P2.5	154.98	3.96	158.27	2.50%
P2.6	157.77	3.94	161.30	2.45%
Average	155.06	3.90	158.57	2.46%
St. Dev	2.87	0.10	2.90	

The net efficiency over the entire test is finally calculated as

$$\eta_{net} = \frac{E_{net}}{m^*_{H_2 in} LHV} \tag{10}$$

With

$$E_{net} = \int_0^{t_{test}} P_{net}\, dt \tag{11}$$

To highlight the additional inefficiencies introduced by fan parasitic power and purge losses, the net efficiency is compared with the stack efficiency, defined as

$$\eta_{stack} = \frac{E_{stack}}{m_{H_2 th} LHV} \tag{12}$$

Figure 22 compares the average values of voltaic efficiency, stack efficiency, and net efficiency for the six repetitions of test P2. Literature values of utilization factor (92%) were used to assess the net efficiency, since the measured flow rate of hydrogen was not accurate. On average, the net efficiency is 52.2%, while the stack efficiency is 58%. The fan alone reduces the stack efficiency by 1.3 percentage points, on average.

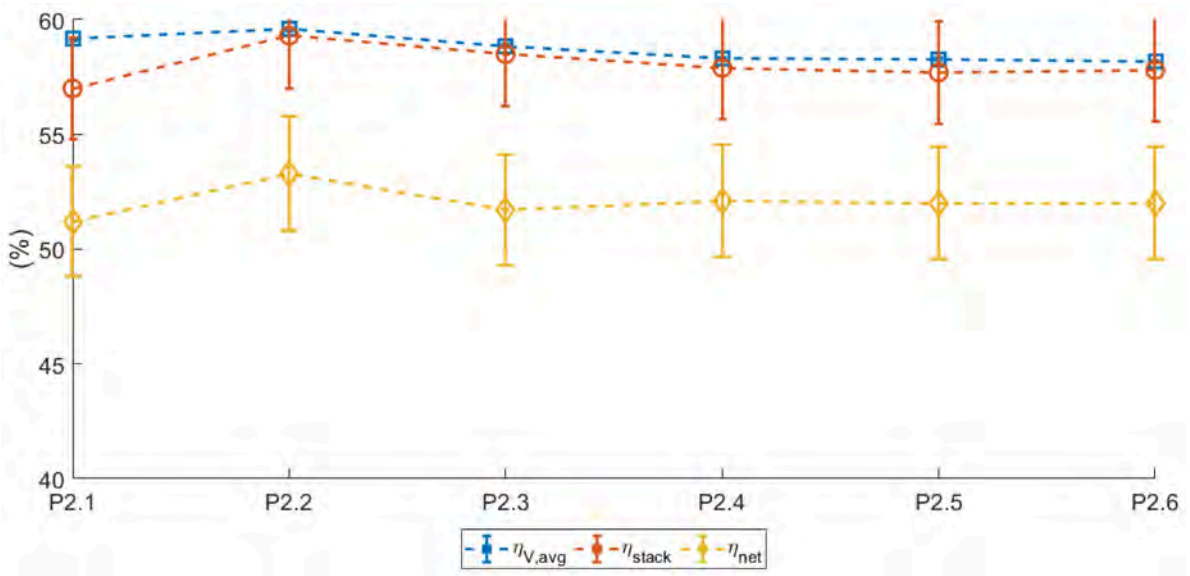

Figure 22. Comparison between voltaic, stack, and net efficiency with estimated error bars.

The error bands shown in the plots represent the estimated uncertainty associated with each efficiency value, calculated using the error propagation methodology described in [52]. The average estimated relative uncertainty in net power is approximately 4.2%, whereas the average relative uncertainty in fan power is about 2%, based on the accuracies of the voltage and current measurements. Since the performance metrics defined in Equations (10)–(12) are based on time-integrated quantities, the corresponding relative uncertainties are 3.9% and 4.7% for stack energy and net energy, respectively, based on an average relative uncertainty of 2.7% for the hydrogen measurement.

The Sankey diagram of Figure 23 illustrates the energy flows within the fuel cell system using the average values of purge losses, stack efficiency, and net efficiency based on the average values of Figure 22.

Although the losses due to cooling fans and purge events are relatively small, this analysis highlights the importance of a comprehensive estimation of hydrogen consumption and net efficiency for an accurate assessment of endurance. Assuming that the drone is equipped with a tank containing exactly 8.2 g of hydrogen (equal to the average value of $m_{H_2,th}$), it would not be able to complete the 25 min mission, as the hydrogen supply would be depleted before due to purge losses and fan parasitic power.

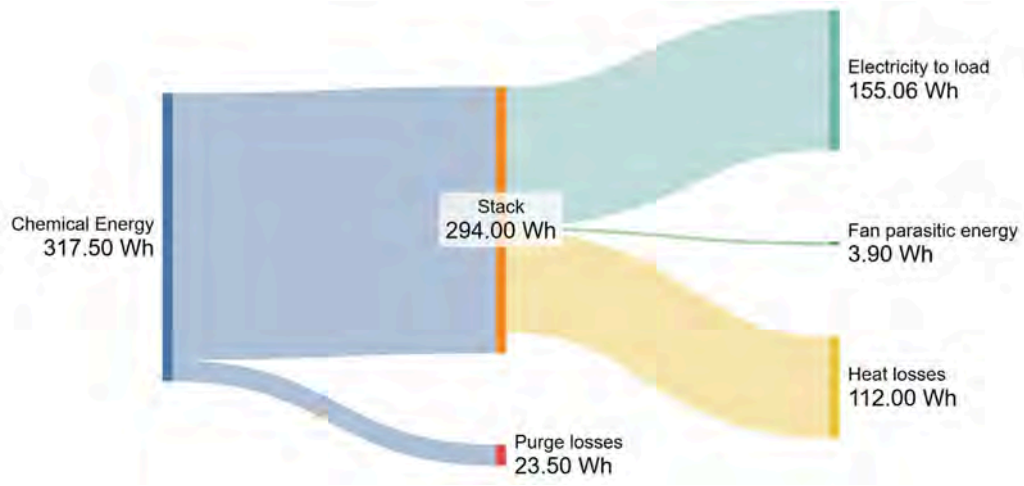

Figure 23. Sankey diagram of the average energy flows in the FCS during the test P2.

6. Conclusions

This study demonstrates that the performance of open-cathode PEM fuel cell systems under realistic dynamic operation significantly deviates from steady-state predictions due to the combined effects of thermal inertia, balance-of-plant dynamics, and purge-related losses. Experimental results show that rapid load variations induce temperature hysteresis and delayed thermal stabilization, leading to voltage deviations of up to ±5% from steady-state values.

A system-level analysis reveals that auxiliary components and purge events, although often neglected, have a measurable impact on overall performance and endurance. Under flight-representative operating conditions, the system achieved an average voltaic efficiency ranging from 55.3% to 60.7%, with a corresponding net efficiency between 50.2% and 54.2%. The cathode fan consumed approximately 2.5% of the stack energy output. Net efficiency was estimated using hydrogen utilization factors reported in the literature, since the uncertainty associated with the hydrogen flow measurements prevented a reliable quantification of hydrogen losses related to purge events and SCU operation. These results highlight that neglecting such effects leads to a systematic overestimation of hydrogen efficiency and mission endurance.

From an engineering perspective, the findings emphasize the need for an energy-based approach to accurately assess fuel consumption in dynamic applications, like those encountered in drones and small vehicles. In particular, endurance estimation and tank sizing should include a design margin of at least 10% to account for auxiliary loads and purge losses. Furthermore, the results underline the importance of optimizing fan control strategies under transient conditions and adapting purge management to variable load profiles. The proposed energy-based framework provides a practical methodology for translating stack-level measurements into realistic estimates of vehicle-level endurance, while systematically accounting for auxiliary loads, transient effects, and hydrogen utilization losses.

The role of the supercapacitor was confirmed to be beneficial in mitigating rapid load transients by reducing the rate of change of stack current, although it does not fully eliminate high-frequency fluctuations. This indicates that passive hybridization alone may be insufficient for highly dynamic missions.

The study also highlights important experimental limitations. Tests were conducted under uncontrolled ambient conditions, and hydrogen mass flow measurements were affected by calibration issues, restricting quantitative analysis to a conservative estimation framework. Future work will address these limitations through experiments in a controlled

altitude chamber and the implementation of improved high-frequency and calibrated measurement systems, enabling a more rigorous quantification of dynamic hydrogen consumption and system efficiency.

Author Contributions: Conceptualization, T.D.; methodology, T.D. and A.G.B.; software, T.D.; validation, A.M.; formal analysis, T.D. and A.M.; investigation, T.D. and A.G.B.; resources, T.D. and A.F.; data curation, A.G.B. and A.M.; writing—original draft preparation, T.D. and A.G.B.; writing—review and editing, T.D.; visualization, T.D.; supervision, T.D. and A.M.; project administration, A.F.; funding acquisition, A.F. All authors have read and agreed to the published version of the manuscript.

Funding: The numerical investigation has been supported under the National Recovery and Resilience Plan (NRRP), Mission4 Component 2 Investment 1.4-Call for tender No. 3138 of 16 December 2021 of the Italian Ministry of University and Research, financed by the European Union-NextGenerationEU (AwardNumber: National Sustainable Mobility Center CN00000023, named MOST, Concession Decree No. 1033 of 17 June 2022), adopted by the Italian Ministry of University and Research, Spoke 14 "Hydrogen and New Fuels". The experimental research activity was founded by the Department of Engineering for Innovation at the University of Salento, with resources provided by the Italian Ministry of University and Research, Art. 238, paragraph 5 of Decree-Law No. 34 of 19 May 2020 (converted with amendments by Law No. 77 of 17 July 2020).

Institutional Review Board Statement: Not applicable.

Informed Consent Statement: Not applicable.

Data Availability Statement: The original contributions presented in this study are included in the article. Further inquiries can be directed to the corresponding author.

Acknowledgments: The authors would like to thank DTA-Scarl (regional district for aeronautics) and, in particular, Stefano Guagnano, for the acquisition of experimental data on the quadcopter.

Conflicts of Interest: The authors declare no conflicts of interest.

Abbreviations

The following abbreviations are used in this manuscript:

BOP	Balance of Plant
DC	Direct Current
FCS	Fuel Cell System
MEA	Membrane Electrode Assembly
PEM or PEMFC	Proton Exchange Membrane Fuel Cell
SCU	Short Circuit Unit
UAV	Unmanned Aerial Vehicle
UC	Ultracapacitor

References

1. Xu, L.; Huangfu, Y.; Ma, R.; Xie, R.; Song, Z.; Zhao, D.; Yang, Y.; Wang, Y.; Xu, L. A Comprehensive Review on Fuel Cell UAV Key Technologies: Propulsion System, Management Strategy, and Design Procedure. *IEEE Trans. Transp. Electrif.* **2022**, *8*, 4118–4139. [CrossRef]
2. Singh, S.; Chaudhari, C.; Sundarraman, M.; Sonkar, K.; Bera, T.; Badhe, R.; Srivastva, U.; Sharma, A. *Proceedings of the Air-Cooled Fuel Cell for Low Power Mobility Application, Pune, India, 16 January 2026*; SAE International: Warrendale, PA, USA, 2026; p. 2026-26-0255.
3. Donateo, T.; Pacella, D.; Indiveri, G.; Ingrosso, F.; Damiani, A. Dynamic Modeling of a PEM Fuel Cell for a Low Consumption Prototype. *SAE Tech. Pap.* **2013**, *2*, 10.
4. Figueroa-Santos, M.; Sulzer, V.; Kim, Y.; Siegel, J.; Stefanopoulou, A.; Rizzo, D.M. Airflow and Power-Split Control Strategy for a Fuel Cell Hybrid Powered Robot. *IFAC-Pap. OnLine* **2021**, *54*, 387–392. [CrossRef]

5. Donateo, T.; Pacella, D.; Laforgia, D. Experimental Test of a GA-Optimized Control Strategy on the H2-VOLKS demonstrator. In Proceedings of the Third European Fuel Cell Technology and Applications Conference, Rome, Italy, 15–18 December 2009; pp. 29–30.
6. Sekhar, Y.C.; Cho, S. Advances in Methanol Oxidation Catalysts and System-Level Engineering for Direct Methanol Fuel Cells. *Chem. Commun.* **2026**, *62*, 7925–7942. [CrossRef]
7. Donateo, T.; Ficarella, A.; Lecce, L. *Preliminary Design of a Retrofitted Ultralight Aircraft with a Hybrid Electric Fuel Cell Power System*; IOP Publishing: Bristol, UK, 2024; Volume 2716.
8. He, Y.; Hu, P.; Cao, Z.; Wang, K.; Ge, Z.; Qi, L.; Zeng, S.; Zheng, J.; Shi, J. Comparative Endurance Evaluation of Hydrogen Fuel Cell and Battery-Electric Propulsion Systems for Small Commercial Unmanned Aerial Vehicles. *J. Energy Storage* **2026**, *161*, 121813. [CrossRef]
9. Xiao, C.; Wang, B.; Zhao, D.; Wang, C. Comprehensive Investigation on Lithium Batteries for Electric and Hybrid-Electric Unmanned Aerial Vehicle Applications. *Therm. Sci. Eng. Prog.* **2023**, *38*, 101677. [CrossRef]
10. Abdulrahman, G.A.Q.; Qasem, N.A.A.; Abdelrahman, W.G.; Abdallah, A.M. A Review of Powering Unmanned Aerial Vehicles by Clean and Renewable Energy Technologies. *Sustain. Energy Technol. Assess.* **2025**, *73*, 104150. [CrossRef]
11. Sekhar, Y.C.; Cho, S. Single-Atom Catalysts for Fuel-Cell Cathodes: Atomic-Level Design, Mechanistic Insights, and Practical Challenges. *Processes* **2026**, *14*, 1473. [CrossRef]
12. Larminie, J.; Dicks, A.; McDonald, M.S. *Fuel Cell Systems Explained*; Wiley: Chichester, UK, 2003.
13. Donateo, T. Simulation Approaches and Validation Issues for Open-Cathode Fuel Cell Systems in Manned and Unmanned Aerial Vehicles. *Energies* **2024**, *17*, 900. [CrossRef]
14. Squadrito, G.; Maggio, G.; Passalacqua, E.; Lufrano, F.; Patti, A. An Empirical Equation for Polymer Electrolyte Fuel Cell (PEFC) Behaviour. *J. Appl. Electrochem.* **1999**, *29*, 1449–1455. [CrossRef]
15. Mirfarsi, S.H.; Parnian, M.J.; Rowshanzamir, S. Self-Humidifying Proton Exchange Membranes for Fuel Cell Applications: Advances and Challenges. *Processes* **2020**, *8*, 1069. [CrossRef]
16. Zhang, C.; Liu, H.; Zeng, T.; Chen, J.; Lin, P.; Deng, B.; Liu, F.; Zheng, Y. Systematic Study of Short Circuit Activation on the Performance of PEM Fuel Cell. *Int. J. Hydrogen Energy* **2021**, *46*, 23489–23497. [CrossRef]
17. Trogadas, P.; Cho, J.I.S.; Kapil, N.; Rasha, L.; Corredera, A.; Brett, D.J.L.; Coppens, M.-O. Effect of Extended Short-Circuiting in Proton Exchange Membrane Fuel Cells. *Sustain. Energy Fuels* **2020**, *4*, 5739–5746. [CrossRef]
18. Kim, J.; Kim, D.-M.; Kim, S.-Y.; Nam, S.W.; Kim, T. Humidification of Polymer Electrolyte Membrane Fuel Cell Using Short Circuit Control for Unmanned Aerial Vehicle Applications. *Int. J. Hydrogen Energy* **2014**, *39*, 7925–7930. [CrossRef]
19. Harel, F.; Gustin, F.; Mainka, J.; Wu, P. Effects of Short Circuit Applications on PEM Fuel Cell Performance and Degradation. *J. Power Sources* **2025**, *632*, 236348. [CrossRef]
20. Niu, T.; Yu, X.; Zhang, C.; Wang, G.; Han, M.; Liu, H.; Zhao, F.; Shuai, Q. Purge Strategy Analysis of Proton Exchange Membrane Fuel Cells Based on Experiments and Comprehensive Evaluation Method. *Fuel* **2024**, *363*, 130970. [CrossRef]
21. Munsi, M.S.; Joshi, R.P. Comprehensive Analysis of Fuel Cell Electric Vehicles: Challenges, Powertrain Configurations, and Energy Management Systems. *IEEE Access* **2024**, *12*, 145459–145482. [CrossRef]
22. Strahl, S.; Husar, A.; Puleston, P.; Riera, J. Performance Improvement by Temperature Control of an Open-Cathode PEM Fuel Cell System. *Fuel Cells* **2014**, *14*, 466–478. [CrossRef]
23. Bradley, T.H.; Moffitt, B.A.; Mavris, D.N.; Parekh, D.E. Development and Experimental Characterization of a Fuel Cell Powered Aircraft. *J. Power Sources* **2007**, *171*, 793–801. [CrossRef]
24. Boukoberine, M.N.; Donateo, T.; Benbouzid, M. Optimized Energy Management Strategy for Hybrid Fuel Cell Powered Drones in Persistent Missions Using Real Flight Test Data. *IEEE Trans. Energy Convers.* **2022**, *37*, 2080–2091. [CrossRef]
25. Boukoberine, M.N.; Zia, M.F.; Benbouzid, M.; Zhou, Z.; Donateo, T. Hybrid Fuel Cell Powered Drones Energy Management Strategy Improvement and Hydrogen Saving Using Real Flight Test Data. *Energy Convers. Manag.* **2021**, *236*, 113987. [CrossRef]
26. Çınar, H.; Kandemir, I.; Donateo, T. Current Technologies and Future Trends of Hydrogen Propulsion Systems in Hybrid Small Unmanned Aerial Vehicles. In *Hydrogen Electrical Vehicles*; John Wiley & Sons, Inc.: Hoboken, NJ, USA, 2022; pp. 75–109.
27. Santos, D.F.M.; Ferreira, R.B.; Falcão, D.S.; Pinto, A.M.F.R. Evaluation of a Fuel Cell System Designed for Unmanned Aerial Vehicles. *Energy* **2022**, *253*, 124099. [CrossRef]
28. Zhao, D.; Xia, L.; Dang, H.; Wu, Z.; Li, H. Design and Control of Air Supply System for PEMFC UAV Based on Dynamic Decoupling Strategy. *Energy Convers. Manag.* **2022**, *253*, 115159. [CrossRef]
29. Pukrushpan, J.T.; Peng, H.; Stefanopoulou, A.G. Simulation and Analysis of Transient Fuel Cell System Performance Based on a Dynamic Reactant Flow Model. In *Proceedings of the Dynamic Systems and Control, New Orleans, LA, USA, 17–22 November 2002*; ASMEDC: New Orleans, LA, USA, 2002; pp. 637–648.
30. Atkinson, R.W.; Hazard, M.W.; Rodgers, J.A.; Stroman, R.O.; Gould, B.D. An Open-Cathode Fuel Cell for Atmospheric Flight. *J. Electrochem. Soc.* **2017**, *164*, F46–F54. [CrossRef]

31. Lin, Y.-F.; Chen, Y.-S. Experimental Study on the Optimal Purge Duration of a Proton Exchange Membrane Fuel Cell with a Dead-Ended Anode. *J. Power Sources* **2017**, *340*, 176–182. [CrossRef]
32. Yang, C.; Moon, S.; Kim, Y. A Fuel Cell/Battery Hybrid Power System for an Unmanned Aerial Vehicle. *J. Mech. Sci. Technol.* **2016**, *30*, 2379–2385. [CrossRef]
33. Tian, W.; Liu, L.; Zhang, X.; Shao, J.; Ge, J. Adaptive Hierarchical Energy Management Strategy for Fuel Cell/Battery Hybrid Electric UAVs. *Aerosp. Sci. Technol.* **2024**, *146*, 108938. [CrossRef]
34. Liu, H.; Cui, H.; Ma, D. Design and Optimization of Hydrogen Fuel Cell-Powered Aerial Vehicles for Urban Air Mobility. *Case Stud. Therm. Eng.* **2025**, *75*, 107006. [CrossRef]
35. Zhang, C.; Liu, Z.; Zhou, W.; Chan, S.H.; Wang, Y. Dynamic Performance of a High-Temperature PEM Fuel Cell—An Experimental Study. *Energy* **2015**, *90*, 1949–1955. [CrossRef]
36. Hou, Y.; Zhuang, M.; Wan, G. A Transient Semi-Empirical Voltage Model of a Fuel Cell Stack ⋆. *Int. J. Hydrogen Energy* **2007**, *32*, 857–862. [CrossRef]
37. Tang, Y.; Yuan, W.; Pan, M.; Li, Z.; Chen, G.; Li, Y. Experimental Investigation of Dynamic Performance and Transient Responses of a kW-Class PEM Fuel Cell Stack under Various Load Changes. *Appl. Energy* **2010**, *87*, 1410–1417. [CrossRef]
38. Marqués, R.; Montero, Á.; Sánchez-Diaz, C.; Quintanilla, I. Design Methodology and Simulation Analysis of Hybrid Fuel Cell and Battery Systems for Powering Unmanned Aircraft Systems. *Energy Convers. Manag.* **2024**, *306*, 118303. [CrossRef]
39. Meng, H.; Yu, X.; Luo, X.; Tu, Z. Modelling and Operation Characteristics of Air-Cooled PEMFC with Metallic Bipolar Plate Used in Unmanned Aerial Vehicle. *Energy* **2024**, *300*, 131559. [CrossRef]
40. Zine, Y.; Benmouna, A.; Becherif, M.; Hissel, D. Towards Maximum Efficiency of an Open-Cathode PEM Fuel Cell System: A Comparative Experimental Demonstration. *Int. J. Hydrogen Energy* **2024**, *86*, 72–85. [CrossRef]
41. Ferreira, R.B.; Santos, D.F.M.; Pinto, A.M.F.R.; Falcão, D.S. Development and Testing of a PEM Fuel Cell Stack Envisioning Unmanned Aerial Vehicles Applications. *Int. J. Hydrogen Energy* **2024**, *51*, 1345–1353. [CrossRef]
42. Donateo, T.; Bonatesta, A.G.; Ficarella, A. Holistic Dynamic Modeling of Open-Cathode PEM Fuel Cells for Sustainable Hydrogen Propulsion in UAVs. *Sustainability* **2025**, *18*, 163. [CrossRef]
43. Liu, Z.; Zhou, Q.; Sun, P.; Xu, S. A Multitask Learning Framework With LSTM-TPA for Dynamic Modeling of Automotive Fuel Cell Systems. *IEEE Trans. Transp. Electrif.* **2026**, *12*, 1532–1542. [CrossRef]
44. Kosaka, M.; Uda, H.; Bamba, E.; Shibata, H. Dynamic System Identification Using a Step Input. *J. Low Freq. Noise Vib. Act. Control* **2005**, *24*, 125–134. [CrossRef]
45. Strahl, S.; Husar, A.; Riera, J. Experimental Study of Hydrogen Purge Effects on Performance and Efficiency of an Open-Cathode Proton Exchange Membrane Fuel Cell System. *J. Power Sources* **2014**, *248*, 474–482. [CrossRef]
46. Zhu, Y.; Zou, J.; Li, S.; Peng, C. An Adaptive Sliding Mode Observer Based Near-Optimal OER Tracking Control Approach for PEMFC under Dynamic Operation Condition. *Int. J. Hydrogen Energy* **2022**, *47*, 1157–1171. [CrossRef]
47. Wang, Y.-X.; Qin, F.-F.; Ou, K.; Kim, Y.-B. Temperature Control for a Polymer Electrolyte Membrane Fuel Cell by Using Fuzzy Rule. *IEEE Trans. Energy Conver.* **2016**, *31*, 667–675. [CrossRef]
48. Zhang, B.; Lin, F.; Zhang, C.; Liao, R.; Wang, Y.-X. Design and Implementation of Model Predictive Control for an Open-Cathode Fuel Cell Thermal Management System. *Renew. Energy* **2020**, *154*, 1014–1024. [CrossRef]
49. Djerioui, A.; Houari, A.; Zeghlache, S.; Saim, A.; Benkhoris, M.F.; Mesbahi, T.; Machmoum, M. Energy Management Strategy of Supercapacitor/Fuel Cell Energy Storage Devices for Vehicle Applications. *Int. J. Hydrogen Energy* **2019**, *44*, 23416–23428. [CrossRef]
50. Hoogendoorn, J. Fuel Cells and Battery Hybrid System Optimization. Master's Thesis, U Delft Aerospace, Delft, The Netherlands, 2018.
51. Li, Y.; Liu, Y.; Han, L.; Liang, Q.; Wan, N.; Guo, Z. Preparation and Application of a kW-Level Air-Cooled PEMFC Stack with Titanium Bipolar Plates for UAVs. *Int. J. Hydrogen Energy* **2025**, *139*, 396–402. [CrossRef]
52. Taylor, J.R. *An Introduction to Error Analysis: The Study of Uncertainties in Physical Measurements*; MIT Press: Cambridge, MA, USA, 2022.